ACS OMEGA

Open Access

http://pubs.acs.org/journal/acsodf

Article

Intermediate-Controlled Synthesis of Quasi-2D $(PEA)_2MA_4Pb_5I_{16}$ in the 20−30% Relative Humidity Glovebox Environment for Fabricating Perovskite Solar Cells with 1 Month Durability in the Air

Yen-Shuo Chen, Min-Han Hsieh, Ching-Chang Lin, Yi-Cheng Huang, Shang-Yu Tsai, and Fu-Hsiang Ko*

Cite This: *ACS Omega* 2024, 9, 48374−48389

Read Online

ACCESS | Metrics & More | Article Recommendations | Supporting Information

ABSTRACT: Herein, quasi-two-dimensional (Q-2D) $(PEA)_2MA_4Pb_5I_{16}$ (prepared by a two-step process) and hole transport layer of a solar cell were fabricated in a high relative humidity (25 ± 5%) environment. The PSC behavior of most Q-2D perovskites is worse than that of three-dimensional perovskites owing to the horizontal alignment of the innate characteristic organic plates on the substrate. Using hybrid immersion solvents (HISs), we have improved vertical alignment in an appropriate ratio to enhance the efficiency of charge transfer and the high coverage of the first priming layer (first step). The grazing incidence X-ray diffraction pattern of the optimized structures revealed a preferential orientation for the vertical alignment of (111), which improved the charge transfer in PSCs and micrometer-level grain size growth. The second step was processed in a high-humidity environment (50 ± 5%) (methylammonium iodide solution embedded), and Q-2D $(PEA)_2MA_4Pb_5I_{16}$ demonstrated distinct grain boundaries. The power conversion efficiency (PCE, 13.09%) of the champion device of the first priming layer prepared using the HIS system increased by >55% compared to the single-immersion solvent (8.3%). The PCE of the ion-modified ETL PSCs was 16.02% (CsF-3) and 14.58% (CsCl-3) and demonstrated 22 and 11% improvement, respectively. The ion-modified electron transport layer (ETL) was deposited in the air, which reduced the power consumption of preparing perovskite solar cells (PSCs). Finally, all Q-2D PSCs were stored in the air, and three PSCs (DMF/DMSO, CsF-3, and CsCl-3) using HIS exhibited long-term stability for 1 month maintaining 80−88% of PCE, demonstrating the importance of the HIS system to improve the first step of growth orientation, which enhances the stability and photovoltaic properties of PSCs.

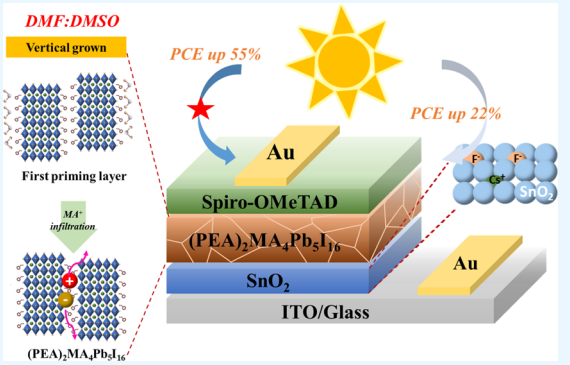

INTRODUCTION

Quasi-two-dimensional (Q-2D) Ruddlesden−Popper layered metal halide perovskites are of interest because of their better photoelectric properties, higher moisture stability, and lower light-induced degradation, and they are often compared with three-dimensional (3D) perovskite materials.[1−5] The hydrophobic organic spacer cations allow excellent interlocking between organic and inorganic substances.[6] The general chemical formula of the Q-2D layered perovskite is $A_2B_{n-1}M_nX_{3n+1}$ (n = 1, 2, 3, 4, ...), where A is a long-chain organic cation (spacer) [butylammonium (BA^+) or phenylethylammonium (PEA^+)],[7−9] B is a short-chain organic cation [methylammonium (MA^+) and formamidinium (FA^+)],[10] M is a divalent metal cation (Pb^{2+} or Sn^{2+}), X is a halide anion (I^-, Cl^-, or Br^-), and n represents the number of inorganic $[MX_6]^{4-}$ octahedral layers separated between the interdigitating bilayers of intercalated bulky alkylammonium cations.[11,12]

The underutilization of sunlight in Ruddlesden−Popper phase Q-2D perovskites is because of their sandwich-like structure, where organic spacer cations parallel to the substrate limit the charge carrier from transferring between the adjacent inorganic octahedral layers.[11] The strong difference in dielectric constants between the organic and inorganic layers induces the formation of excitons with considerable binding energy and low carrier mobility. This results in an increased rate of charge recombination before being collected, which hinders the perovskite solar cell (PSC) performance.[13] Although economically viable processing conditions and environmental stability have popularized Q-2D PSCs, the photovoltaic properties of Q-2D perovskites must be optimized for innate shortcomings to achieve high power conversion efficiency (PCE).[14] Preferred crystallographic

Received: July 17, 2024
Revised: November 17, 2024
Accepted: November 21, 2024
Published: November 27, 2024

orientations are obtained through solution-engineered modification of the crystallization process of Q-2D perovskite films (PFs), such as hot casting,[15,16] additive engineering, and thermally aged precursor solution-treated film growth to facilitate charge transport.[8,17,18] $(PEA)_2MA_4Pb_5I_{16}$ (PMPI) films with organic cations preferentially oriented perpendicular to the substrate were obtained by Gao et al. by controlling the growth of the intermediate phase in a cosolvent.[19] Several methods for improving the crystal growth orientation are reported.[20−22] Li et al. reduced the nucleation sites in the solution via thermal aging of the solution to trigger colloidal aggregation, which formed a dense Q-2D PF with 18.68% PCE.[23] Yue et al. deposited Q-2D $(AA)_2MA_4Pb_5I_{16}$ via nontoxic acetic acid as a cosolvent. The strong power-supplying ability of acetic acid with the critical component led to iodide-induced favorable cluster aggregation. Consequently, it regulated the crystal growth with increased photovoltaic efficiency (18.55%).[24] The study demonstrated a breakthrough in photovoltaic performance through solution improvement of Q-2D PSCs. However, two-step deposition is considered a controlled and reliable method to synthesize highly uniform perovskite components for large-scale applications.[25] The main advantage of two-step solution deposition over one-step deposition is its reproducibility,[26] which is one of the most critical metrics for commercialization.

Tai et al. reported the use of the $Pb(SCN)_2$ precursor in preparing the $CH_3NH_3PbI_{3-x}(SCN)_x$ layer in ambient air. The PSCs fabricated with this method demonstrated improved stability in humid environments and achieved a PCE of over 15%.[27] Lai et al. reported that Q-2D PF made with fluorinated benzylammonium iodide achieved a PCE of about 20% at a relative humidity (RH) of ∼20%.[4] Ke et al. reported applying a layered $(PEA)_2FA_2Pb_nI_{3n+1}$ perovskite light absorber via a two-step process with enhanced stability in humid conditions for solar cell applications with 11.46% PCE. It retained 86% of the initial PCE after exposure to RH of up to 60% for nearly 900 h.[28] Lu et al. demonstrated the growth of FA-based Ruddlesden−Popper-type perovskites $M_2FA_{n-1}Pb_nI_{3n+1}$ via a two-step sequential deposition process. $FA_2FA_{n-1}PbnI_{3n+1}$ was formed with the benzylamine (PMAI) ratio increase in the second step with >19% PCE.[29] Wu et al. discussed the importance of the priming layer for 3D perovskites.[30] PbI_2 was treated with a strong ligand solvent [dimethyl sulfoxide (DMSO)] (first step) to generate homogeneous thin films effectively. The first step of preparing primer layers using mixed immersion solvents with different solvent ratios was characterized to adjust the coordination and coverage rates of PbI_2 and phenethylammonium iodide (PEAI).

Recently, the net-zero issue has received extensive attention. According to the Paris Agreement[31] and the Carbon Border Adjustment Mechanism (CBAM),[32] heavy industries, buildings, and mining should adopt comprehensive approaches to reduce emissions, and the research and industrial sectors should comply with carbon (or carbon dioxide) management in the future.[33] The solar, renewable energy industry can control carbon emissions by replacing high-carbon emitting equipment. However, most PSCs are manufactured and stored in energy-consuming gloveboxes, which is challenging. Herein, we use nitrogen gloveboxes to control RH (25−75%) in the absence of electricity instead of the moisture-, volume-, concentration-, and humidity-controlled power-consuming equipment. We propose a two-step method for fabricating Q-2D PMPI (MA = methylammonium) as light-absorbing materials for solar cells. Perovskite and the hole transport layer (HTL) are manufactured in high RH (25 ± 5%), and the electron transport layer (ETL) is manufactured in the air. The difference in coordination between *N*,*N*-dimethylformamide (DMF), DMSO, and Pb^{2+} in the precursor was exploited in the first step to investigate the optimal mixing ratio of the HIS to obtain a high coverage and large grain size of active materials. The first step formed a vertically aligned (111) as a primer layer. MA^+ can easily enter the primer layer and self-assemble to form the (111) oriented Q-2D $(PEA)_2MA_4Pb_5I_{16}$ film in the second step owing to the layered structure. We have previously reported the post-treatment of perovskite with ionic solutions to enhance electrical properties.[34] In this study, SnO_2 as the ETL was optimized by using ultralow-temperature ionic solutions (CsF and CsCl) to improve the carrier concentration of SnO_2. Q-2D $(PEA)_2MA_4Pb_5I_{16}$ (PMPI) films with few defects, large grains, and a regular arrangement were obtained in the HIS. The photovoltaic efficiency (13.09%) of the solar cell was highly improved, with a 57% increase in the PCE compared to that of the DMSO-based PSC (8.3%). The PCEs of CsF- and CsCl-modified ETL-based PSCs were 16.02 and 14.58%, respectively. The durability of the device with the optimized structure was 4 weeks and maintained a higher PCE of 81−87% than those of PSCs based on a single solvent.

EXPERIMENTAL SECTION

Materials. The chemicals were used as purchased. Tin oxide (SnO_2, 15% in H_2O colloid dispersion) was purchased from Alfa Aesar. Cesium fluoride (CsF, 99%), cesium chloride (CsCl, 99%), cesium bromide (CsBr, 99%), and cesium iodide (CsI, 99%) were purchased from Sigma-Aldrich. Methylammonium iodide (MAI, >98.0%) was purchased from TCI. Lead iodide (PbI_2, 99.9985%) was purchased from Alfa Aesar. Phenethylammonium iodide (PEAI) was purchased from Greatcell Solar. Spiro-OMeTAD was purchased from Sigma-Aldrich. 4-*Tert*-butylpyridine (TBP, >96%) was purchased from TCI. The patterned ITO glass (∼15 Ω sq^{-1}) was obtained from Lumtec Taiwan, and the ITO substrate was cut into sizes of 2 cm × 3 cm for the experiment.

Solution Preparation. The precursor solution was prepared by diluting 0.5 mL of SnO_2 colloidal solution (15%) in 2 mL of deionized water. 7.5 mg of CsCl, CsBr, CsI, and CsF were dissolved in the dilute SnO_2 solution to obtain CsF, CsCl, CsBr, and CsI (wt %) of 3 mg mL^{-1}, respectively. The Spiro-OMeTAD solution was prepared by mixing 1 mL of Spiro-OMeTAD solution (72.3 mg of Spiro-OMeTAD powder in 1 mL of chlorobenzene) and 17.5 μL of Li-bis-(trifluoromethylsulfonyl)imide (TFSI) solution (520-mg of Li-TFSI powder in 1 mL of acetonitrile). 28.75 μL of tributyl phosphate (TBP) was added to the solution.

Fabrication of the PSC. The glass substrate was ultrasonically cleaned sequentially by using acetone, ethyl alcohol, and deionized water for 15 min. The substrate was dried using N_2 gas, and the glass was treated with O_2 plasma for 3 min to remove residual contaminants adhering to the ITO glass surface. The improved surface wettability of the substrate achieved a better solution coverage for the spin-coating procedure. The SnO_2 ETL was fabricated using the solution method. The precursor was prepared by diluting SnO_2 solution (15%) in deionized water and adding CsF and CsCl to achieve different weight percentages of interest. The concentrations of CsF and CsCl used in this experiment were 1, 2, 3, 4, and 5 mg mL^{-1}. After that, the solution was

https://doi.org/10.1021/acsomega.4c06621
ACS Omega 2024, 9, 48374−48389

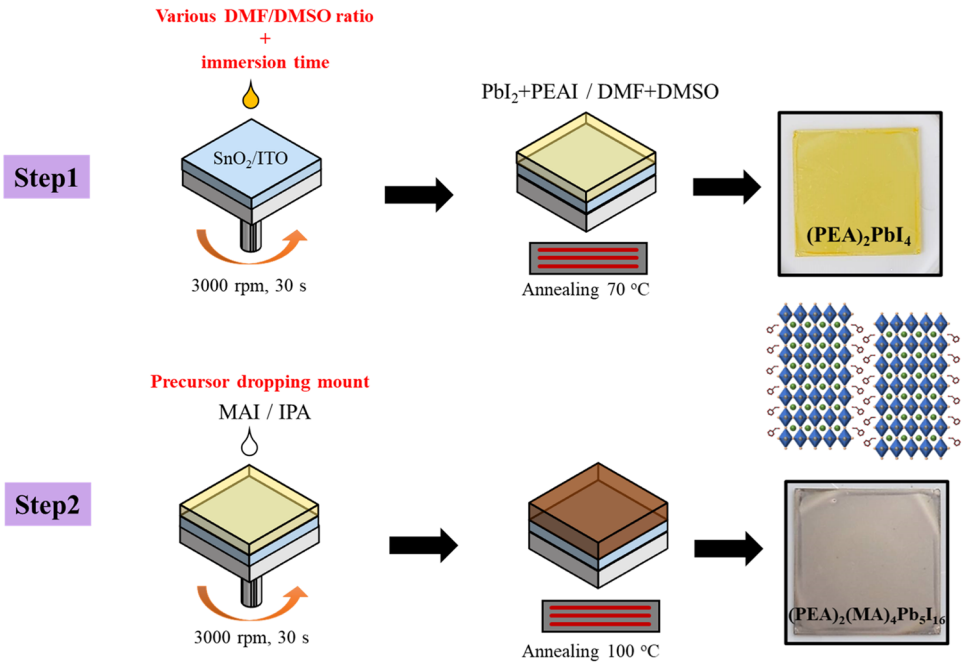

Figure 1. Schematic illustration of the two-step fabrication process for the Q-2D PMPI perovskite under ambient air conditions with high RH.

spin-coated on precleaned ITO glass, followed by annealing in air at 60 °C for 30 min to obtain a modified ETL. The ETL surface undergoes 3 min of O_2 plasma treatment again. The absorbing layer in this study, Q-2D $(PEA)_2MA_4Pb_5I_{16}$ PF, was deposited on the ETL via the two-step solution method. In the first step, the precursor solution was prepared by dissolving PbI_2 and PEAI with mixed solvents of various volume ratios of HIS at a stoichiometric ratio of 5:2 (i.e., 1.0 M Pb^{2+} concentration). The optimal ratio of DMF/DMSO was 8:2 in this experiment. The precursor solution was spin-coated on an ETL glass at 3000 rpm for 30 s. The deposited films were annealed on a hot plate at 70 °C for 10 min and cooled to room temperature at 25 °C. The yellow intermediate films comprising a mixture of $(PEA)_2PbI_4$ and PbI_2 were obtained after the first-step process, as shown in Figure 1. In the second step, MAI was dissolved in an isopropyl alcohol solution (20 mg mL^{-1}). The substrate was spun at 3000 rpm for 30 s. At the 15th second, a certain amount of the MAI solution (80−170 μL) was dripped on the substrate slowly. Finally, the PFs were annealed at 100 °C for 20 min. The color of the obtained films turned from yellow to brown, indicating the formation of Q-2D $(PEA)_2MA_4Pb_5I_{16}$ PF. The two-step process flow is shown in Figure 1. Spiro-OMeTAD was used as the HTL to fabricate the Q-2D PSCs. The precursor solution was spin-coated on the Q-2D perovskite layer at 4000 rpm for 30 s to obtain the HTL layer. A 100-nm-thick Au electrode was thermally coated on the HTL layer.

Measurement and Characterization. The SnO_2-based ETL and Q-to-two-dimensional PFs morphology were analyzed via SEM to investigate the influence of different solvent ratios in precursor solutions. EDS was used to analyze the elements in Q-2D PFs to confirm the formation of Q-2D $(PEA)_2MA_{n-1}Pb_nI_{3n+1}$ perovskites. A contact angle was formed when water was dipped on a solid surface, which quantified the wettability of the SnO_2-based ETL surface. The contact angle becomes smaller when water spreads across the surface, indicating a hydrophilic surface. By contrast, the contact angle > 90° indicates a hydrophobic surface. GIXRD was conducted to observe the crystalline structure of the Q-2D PFs with a glancing angle of 1°. The X-ray source was Cu Kα, and the scanning speed was 0.1° s^{-1} with a step size of 0.015°. The full width at half-maximum (FWHM) was analyzed using ORIGIN Gaussian fitting. UV−vis was used to measure the transmittance of the SnO_2-based ETL and the absorbance of the Q-2D PFs. The transmittance of the SnO_2-based ETL played a crucial role in determining the total amount of light absorbed by the absorbing layer. Steady-PL measurement was conducted by using the source wavelength (nm). PL intensity exhibits electron transfer efficiency from the PL to the ETL. AFM was used to observe the surface roughness of the PFs by scanning a tiny cantilever over the sample and measuring the forces between the probe and the surface. XPS was conducted for element composition analysis in the PFs by measuring the kinetic energy of the photoemitted electrons from the surface after the energy of incident X-rays. The Hall measurement system consists of an electromagnet, a Source Measurement Unit (SMU) instrument (KEITHLEY Model 2400), and a four-probe holder. The $I-V$ characteristics of the Q-2D PSCs were measured under air mass (AM) 1.5G irradiation (100 mW cm^{-2}) at room temperature. The PCE and FF of the solar cells were derived from the result. The external quantum efficiency (Optosolar) was measured using the SRF50 system. TRPL was conducted by using a microphotoluminescence system (Spectra Physics).

RESULTS AND DISCUSSION

Vertical Q-2D $(PEA)_2MA_4Pb_5I_{16}$ (PMPI) Perovskite Morphology of the First Priming Layer in 20−30% RH. According to previous reports, high-performance PSCs can be achieved by fine-tuning different ratios of the HIS to control the perovskite crystal growth direction and the micron-sized grain growth.[24,35] The two-step synthesis method creates a reliable morphology of the first primer layer, directly affecting the final performance of the PSCs. We investigated different ratios of DMF to DMSO to form a high-quality first priming layer during the first step in a high RH. The reaction kinetics of

https://doi.org/10.1021/acsomega.4c06621
ACS Omega 2024, 9, 48374−48389

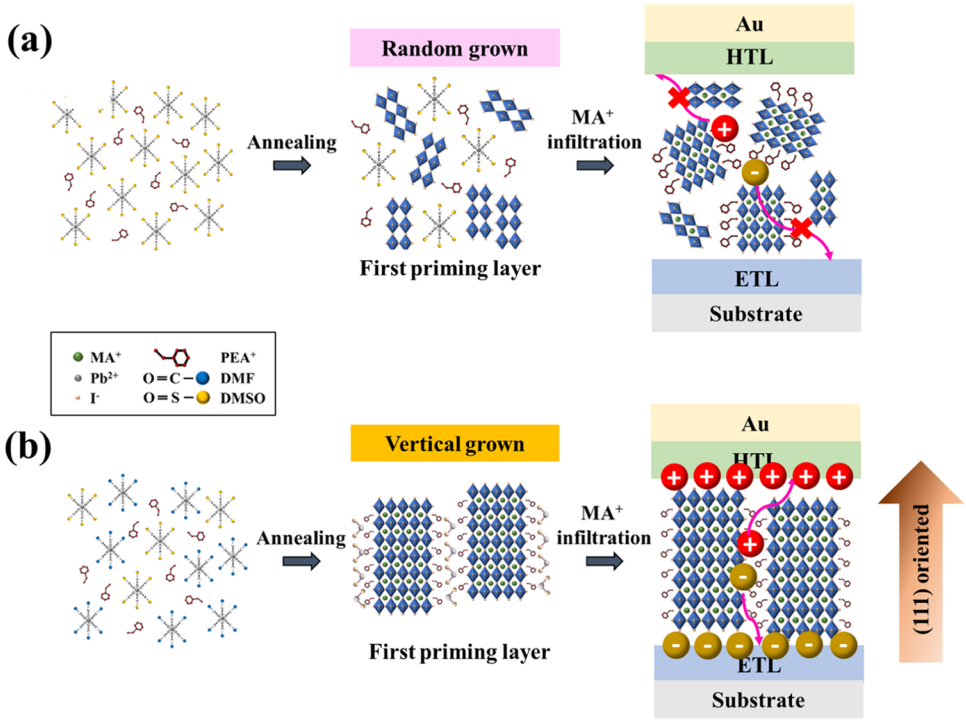

Figure 2. Schematic diagram of the preferential vertically oriented crystallization mechanism and charge-transport channels based on the first priming layer and Q-2D $(PEA)_2MA_4Pb_5I_{16}$ films deposited using (a) DMSO and (b) HIS (DMF/DMSO = 8:2) system.

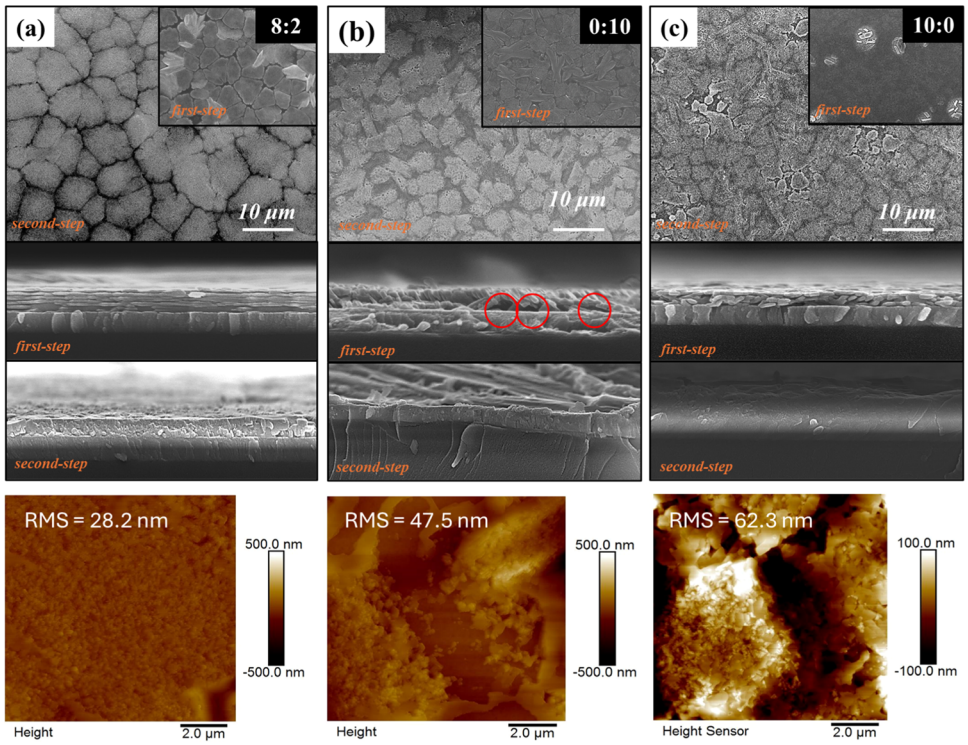

Figure 3. Top-view and cross-sectional SEM and AFM images of the first priming layer. Q-2D $(PEA)_2MA_4Pb_5I_{16}$ films were obtained using (a) DMF/DMSO = 8:2, (b) pure DMSO, and (c) pure DMF.

the Q-2D PFs are related to the interaction between PbI_2 and the coordinating agent (DMF or DMSO). Although single solvents can react with PbI_2 and PEAI to form the first primer layer, the 3D perovskite structural system shows that DMSO has a high affinity for metal halides.[30,36] The coordination of DMSO to Pb^{2+} in the precursor is strong, which might retard the reaction between PbI_2 and PEAI with excess time to release Pb^{2+} and form the first priming layer.[37] The slowed crystallization process makes it difficult for Pb^{2+} to react with other precursors, such as PEA^+, affecting the coverage and forming irregular perovskite structures comprising unwanted PbI_2.[19] The structural mismatch in the Q-2D perovskite layer

https://doi.org/10.1021/acsomega.4c06621
ACS Omega 2024, 9, 48374−48389

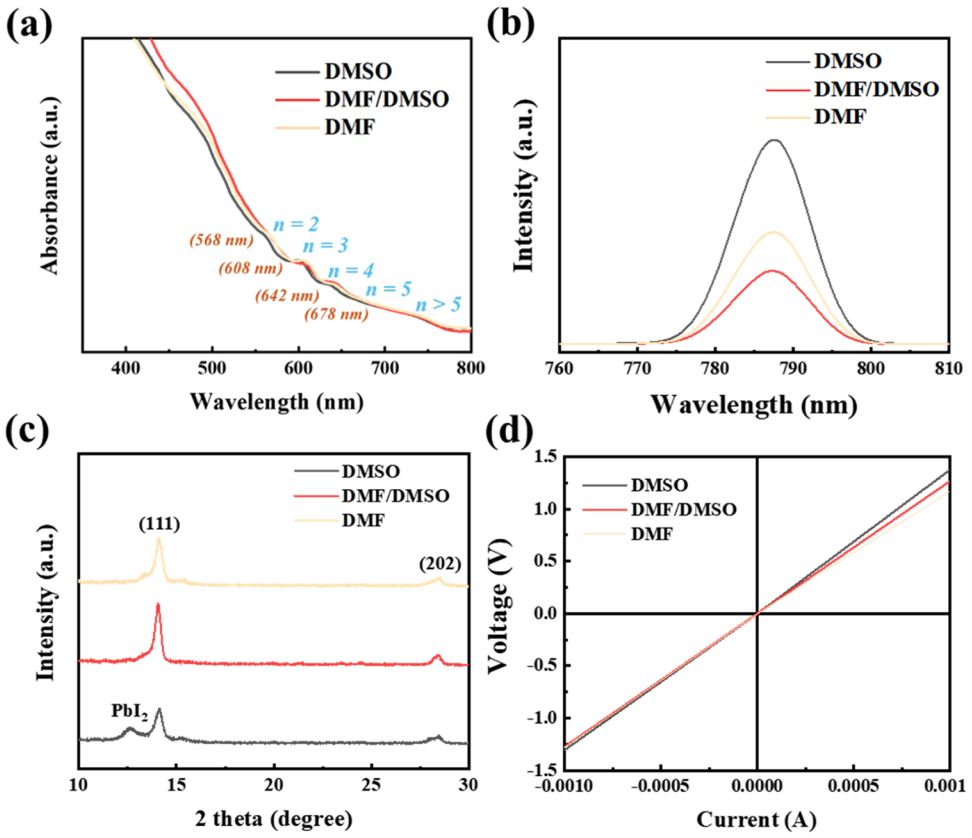

Figure 4. (a) UV−vis absorption spectra, (b) PL spectra, (c) GIXRD patterns, and (d) Hall measurement of Q-2D $(PEA)_2MA_4Pb_5I_{16}$ films deposited on the ITO/substrate using HISs with different solvent ratios.

also restricts charge transfer, which is detrimental to the photovoltaics of PSCs (Figure 2a). Alternately, DMF interacts weakly with Pb^{2+} in the precursor solution, accelerating the reaction between Pb^{2+} and PEA^+ to produce perovskite grains with small sizes and amorphous structures.[38] Adjusting the coordination of DMF/DMSO can selectively induce the crystal growth of the intermediate phase of PFs with a highly preferred (111) orientation usually perpendicular to the substrate surface (Figure 2b), can increase crystallinity and grain sizes, reduce dielectric confinement effects due to the introduction of large organic cations, and enhance charge transfer.

Two-Step Controlled Deposition of the Active Q-2D PMPI Absorption Layer. The uniform covering of the active layer is crucial for the design of highly efficient PSCs. An extended evaporation time localizes solute accumulation with the incomplete coverage of the perovskite layer.[39] Therefore, the effect of the precursor solvent composition on the growth of the Q-2D PMPI crystals was explored. The first priming layer was prepared in a HIS to obtain the best deposition quality and high coverage. The dissolution of the precursor solution in pure DMF is faster than that in pure DMSO owing to the higher polarity of DMSO than DMF (relative solvent polarities of DMSO and DMF are 0.444 and 0.386, respectively).[19] The strong coordination between excess DMSO and Pb^{2+} initiates the first step of dissolving the PbI_2/PEAI precursor, as shown in Figure S1a. The first priming layer comprising pure DMF immediately turned yellow during annealing at 70 °C compared to the first priming layer comprising pure DMSO, which further verifies that the strong polarity of DMSO retards the crystallization rate (Figure S1b). Q-2D PFs were deposited under general acrylic glovebox (RH = 25 ± 5%) conditions rather than under energy-consuming pressure vacuum glovebox (RH < 1 ppm) conditions to investigate the effect of the HIS on PFs and reduce carbon emissions. The first priming layer was characterized to study the influence of the HIS on the formation of grain structures. Figure S2a,b demonstrates that the first priming layer was obtained with DMF:DMSO = 10:0 and 8:2, and immersion time ranging from 5 to 25 s has an optimal 100% coverage of the indium titanium oxide (ITO)/glass substrate (ImageJ Software Analysis). However, increased DMSO content makes the film cover unstable and sensitive to immersion time. The homogeneous substrate coverage of the films obtained by immersing in pure DMF is attributed to the high volatility of DMF (boiling point = 153 °C) compared to DMSO (boiling point = 189 °C).[40,41]

Figure 3 presents the top-view and cross-sectional images of the sample analyzed via scanning electron microscopy (SEM), and the inset shows the first step of preparing the priming layer. The inset in Figure 3a−c shows a standard Q-to-2D film laminate structure with an 8:2 (DMF: DMSO) ratio of the HIS to form high-quality films with a dense and uniform surface morphology. By contrast, cracks with a visible number of pinholes (red circles) and irregular structures are observed in the pure DMSO-based film, while the pure DMF-based films show no discernible structure, which is consistent with a high disorder. The HIS strongly coordinates to form stable intermediate films because it can retard the reaction rate between PEA and PbI_2 in the intermediate film. The first priming layer prepared in DMF:DMSO = 8:2 has a nanoporous morphology as observed from magnified images (Figure S3a), which is favorable for MA^+ penetration and

https://doi.org/10.1021/acsomega.4c06621
ACS Omega 2024, 9, 48374−48389

embedding in the second step of the process.[28] Therefore, HIS instead of a single solvent is necessary to obtain well-crystallized Q-2D PF while maintaining a good substrate coverage in the subsequent process. The ultraviolet−visible (UV−vis) absorption spectrum (Figure S3b) of the Q-2D PF shows high-energy continuous absorption edges and low-energy exciton peaks corresponding to its lowest exciton resonance. Its absorption peak near 520 nm corresponds to the bandgap excitation properties of $(PEA)_2PbI_4$.[42−44] The crystallization of the first priming PFs prepared in the HIS with different solvent ratios was investigated via grazing incidence X-ray diffraction (GIXRD) pattern analyses (Figure S3c). The first primer layer shows distinct peaks at diffraction angles 2θ = 10.8, 16.2, 21.8, 27.33, and 36.2° indexed as a series of reflections of (004), (006), (008), (00$\underline{10}$), and (00$\underline{12}$) of $(PEA)_2PbI_4$, respectively. The results indicate the formation of layered Q-2D PF in the first step, similar to the previously reported XRD patterns of Ruddlesden−Popper crystals with PEAI as the sizable organic cation.[28,45−47]

Figure 3a−c displays the top-view and cross sectional SEM and atomic-force microscopy (AFM) images of Q-2D PMPI films with different solvent-based first priming layers. The surface morphology of the DMF/DMSO-based PF has a larger structure and higher grain size (8.39 μm) than that of the DMSO-based PF (Figure S4a,b) with a more uniform cross section, consistent with fewer internal boundaries and grains with oriented stripes perpendicular to the boundaries. The DMF-based film is irregular after MAI is embedded, owing to the fast crystallization in the first step. Thus, introducing an appropriate amount of DMSO in the first step is crucial for obtaining highly oriented Q-2D crystals. However, an excessive DMSO adversely affects the growth of favorably oriented crystals. SEM images are consistent with the results of AFM measurements. The HIS-based PFs exhibit smoother morphology with lower root-mean-square (RMS) surface roughness (28.2 nm) compared to the PFs synthesized by immersing in pure DMSO and DMF with RMS values of 47.5 and 62.3 nm, respectively.

Figure 4a shows the UV−vis absorption spectra of Q-2D PMPI films in HIS with different solvent ratios for investigating their internal phase distribution. The 568, 608, 642, and 678 nm absorption peaks indicate various exciton peaks associated with different high and low n-values. Thus, the film is a mixture of several n-values that self-organize into a quantum-well structure. The low broad absorption bands in the long wavelength region are attributed to the large $n > 5$ phase.[9,14] The optical bandgap is obtained directly from the Tauc plot (Figure S4c). Q-2D PFs exhibit a similar optical bandgap of 1.8 eV. Figure 4b shows the photoluminescence (PL) spectra of the Q-2D PF, measured on the Q-2D PF/untreated-SnO_2/ITO substrate. The central peak of Q-2D PMPI is located at 786 nm and is generated from the lowest bandgap emission of the high n phase. The PL intensity of the DMF/DMSO-based PF is reduced owing to the vertically aligned crystals facilitating charge transfer and collection, inducing a strong nonradiative loss of photogenerated charge carriers in the PF, which is consistent with the crystal growth mechanism shown in Figure 2b. Figure 4c indicates that the GIXRD patterns of Q-2D PMPI have strong diffraction peaks at 14.1 and 28.2° corresponding to the (111) and (202) planes, respectively. The preferred vertically aligned (111) Q-2D PMPI crystal plane has good photovoltaic properties.[8,11,15] The first priming layer prepared in HIS has a strong intensity. The FWHM of the peak (2θ = 14.1°) in Table 1 decreases from 0.486° (DMF) and 0.437° (DMSO) to 0.326° (DMF/DMSO),

Table 1. FWHM Extracted from Figure 4c for the Comparison of Q-2D PFs in the First Step

HIS ratio (DMF/DMSO)	FWHM (2θ = 14.1°)	FWHM (2θ = 28.4°)
0:10	0.486	0.737
8:2	0.326	0.460
10:0	0.437	0.675

indicating the formation of grain structures, consistent with the morphology changes observed in SEM images. The material is highly disordered, owing to the short crystallization process of the pure DMF-based film deposited in the first step. A relatively broad peak with a high FWHM is observed for the film embedded in the MAI solution, suggesting that Q-2D PMPI comprises unorganized oriented crystals. However, a further increase in the amount of DMSO disrupted the grain structure. The DMSO-based PF shows a distinct PbI_2 peak at 12.7°, confirming that retarding crystallization causes incomplete film transformation. Q-2D PF crystallization depends on the first priming layer deposited in the first step. The Q-2D PMPI was successfully synthesized using a two-step method in a HIS to control the perpendicular growth direction. Improving the film quality and crystallinity improves the electronic and optoelectronic conversion efficiency, and small-angle 2D characteristic peaks are not observed in the GIXRD patterns (in Figure 4c).

Figure S5 reveals the Q-2D PF obtained after the second step with different MAI contents. Q-2D PMPI obtained by the dropwise addition of 110 μL of MAI has the best film quality with nonradiative loss, vertical orientation, and the least amount of unconverted PbI_2. The SEM images with different magnifications further emphasize the formation of lamellar structures as a typical morphology of Q-2D layered materials (Figure S5a−d). The films exhibit square grains similar to Q-2D crystals of graphite or MoS_2, suggesting a perpendicular growth of crystals and confirming that the Q-2D perovskite comprises stacked Q-2D solids.[48] An increase in the MAI solution from 80 to 110 μL decreases the FWHM of the (111) peak considerably from 0.410 to 0.326 (Figure S5e and Table S1). The preferred crystal orientation on the (111) surface corresponds to the growth of Q-2D perovskite crystals perpendicular to the substrate surface, which improves the crystallinity and PCE. Alternately, an increase in the MAI solution from 110 to 170 μL increases the FWHM of (111) to 0.383, which indicates disorder in the PF. The grain boundary is undefined, indicating that the crystallinity of the obtained PF decreases. The XRD results are consistent with the PL spectra (Figure S5f). The PL intensities of the MAI drop amounts were measured on a Q-2D PF/untreated-SnO_2/ITO substrate structure.

Figure 3 shows that the first step of depositing the first priming layer influences the final Q-2D PMPI morphology, and the HIS induces a well-crystallized orientation and film quality. We investigated a second process (MAI solution embedding) in an excessively high humid (from 30 to 60 ± 5% RH) environment to observe the effect on the successive processes of the optimized structure. The surface morphology and grain boundaries of Q-to-Tie-based PMPI deposited in highly humid conditions are distinct (Figure S6) with untransformed PbI_2 and blurred grain-boundary structures.

https://doi.org/10.1021/acsomega.4c06621
ACS Omega 2024, 9, 48374−48389

Table 2. Carrier Density (n), Mobility (μ), Resistivity (ρ), and Conductivity (σ) for Q-2D $(PEA)_2MA_4Pb_5I_{16}$ Films

samples	n (cm^{-3})	μ ($cm^2\ V^{-1}\ s^{-1}$)	ρ (Ω cm)	σ ($S\ cm^{-1}$)
DMSO	5.88×10^{20}	22.3	4.77×10^{-4}	2.10×10^{3}
DMF/DMSO	4.80×10^{20}	39.8	2.97×10^{-4}	3.37×10^{3}
DMF	5.94×10^{20}	35.4	3.27×10^{-4}	3.06×10^{3}

Preliminary demonstration of films with HIS-optimized structures fabricated at high relative humidity.

The Hall measurement was measured to investigate the electrical properties (Figure 4d and Table 2). The electron mobility values of DMSO- and DMF/DMSO-based PFs are 22.3 and 39.8 $cm^2\ V^{-1}\ s^{-1}$, respectively, indicating that the HIS-based PF has the highest electron mobility, in agreement with the PL results. Adjusting the solvent ratio in the HIS can improve the charge transfer efficiency of Q-2D PFs, indicating that the grain structure of Q-2D perovskite facilitates charge carrier transport in PSCs and deposition under highly humid conditions. The grain structure can be achieved by adjusting the coordination strength between PbI_2, DMF, and DMSO, illustrating the importance of optimizing the first priming layer. The distribution of chemical compositions throughout Q-2D HIS-based PF was analyzed via X-ray photoelectron spectroscopy (XPS). The XPS results of Q-2D PMPI show two peaks: Pb $4f_{5/2}$ at 143.5 eV and Pb $4f_{7/2}$ at 138.6 eV. The peaks at 631.2 and 619.5 eV are attributed to I 3d states and agree with the $3d_{3/2}$ and $3d_{5/2}$ states of iodide (Figure S7a,b). Furthermore, no peaks of metallic Pb are observed in the spectra, suggesting the complete conversion of PbI_2 into perovskite.[49] The spectra of C 1s show two peaks at 286.7 and 285.3 eV (Figure S7c). The peak with high binding energy is ascribed to C−N bonding in MA^+, and the peak with low binding energy is from adventitious carbon.[50,51] The results conform with the XPS result of PEA-based perovskite in other reports, confirming the formation of Q-2D PMPI.[52]

Characterization of the Carrier Recombination, Carrier Concentration, Hydrophilicity, and Grain Size of the SnO_2-Based ETL. The ETL−PF interface should be compact and pinhole-free to avoid direct contact between the transparent conducting substrate and the active layer at the PSC interface. Charge recombination is minimized through a suitable energy-level arrangement of the ETL to achieve a high open-circuit voltage (V_{oc}) and short-circuit current. We have reported[34] the effect of passivation defects achieved by post-treating perovskite surfaces with different ionic solutions in the air to explore mechanisms for enhancing the electrical performance of the device. In this study, we systematically investigated the photovoltaic properties of a modified ETL synthesized by doping SnO_2 colloidal solutions with different concentrations of CsF and CsCl ionic solutions. The ETL was annealed at 60 °C. The concentration of CsF immersion solvent is 1 mg mL^{-1}, labeled below as CsF-1, and so on. Figure S8 compares the SEM top-view images of modified ETL obtained at various CsF and CsCl concentrations to the changes in grain sizes. Figure S8a−e demonstrates that the morphologies of pristine SnO_2 and modified films are smooth and homogeneous. The average grain sizes of CsF-SnO_2 and CsCl-SnO_2 films increase with the increase in the concentration of the immersing solvent. The average grain size increases from 10.16 nm (CsF-0) to 14.14 nm (CsF-5) and 17.23 nm (CsCl-5), as calculated using ImageJ software (Figure S8f). The presence of Cs^+, F^-, and Cl^- ions might increase the grain size and decrease the grain boundaries of the SnO_2-treated film.[53] The modified SnO_2 precursor effectively avoids aggregation and forms a film with a uniform coverage. The complete surface coverage of ITO by the ETL is the key to realizing high-performance PSCs in well interfacial contact and conduct with the perovskite layer. Conventional tin dioxide films provide nonwetting surfaces to perovskite precursor solutions and require plasma pretreatment to improve the surface energy of the ETL.[54] The inset of Figure S8 shows the water contact angle measurements of SnO_2 for surface hydrophilicity. The contact angle of the pristine SnO_2 film is 44.6°, while it decreases for the modified SnO_2 film to 3.7° (CsCl-5) and 8.3° (CsF-5). Differences in wettability affect the surface morphology of the perovskite spin-coating process,[55] and the results suggest that CsF- and CsCl-modified ETLs have uniform coverage, nonporous morphology, and high wettability, favorable for the deposition of perovskite layers.

The ETL is compact and pinhole-free with a minimum thickness to minimize the series resistance of PSCs (Figure S9). The cross-sectional SEM images show the ETL thickness values for different concentration modifications. ETLs in all PSCs were spin-coated once on the ITO substrate. The thicknesses of CsF-0-, CsF-5-, and CsCl-5-modified SnO_2 films are 13.8, 25.3, and 20.2 nm, respectively. Although CsF- and CsCl-modified SnO_2 is thin and suitable as an ETL layer, the thickness of the film increases as the concentration of the ionic solution increases. We further measured dynamic light scattering (DLS) to investigate the particle size change and aggregation of SnO_2 in the colloid solution after adding CsF and CsCl to understand the nucleation kinetics of the ETL. The average particle size of the corresponding SnO_2 in CsF and CsCl is shown in Figure S10 and summarized in Table S2. The average particle size of SnO_2 in the pristine colloidal solution is 11.4 nm and increases to 20.4 and 17.7 nm with increasing concentrations of CsF and CsCl, respectively. F^- ions strongly coordinate with Sn^{4+} and adsorbed ions increase individual grain sizes.[56]

SnO_2 nanoparticles aggregate because the electrostatic potential of nanoparticles in colloidal solutions decreases with time. The surface ζ-potentials of CsF-5 and CsCl-5 are −13.17 and −25.56 mV (Figure S11), respectively, with an increasing additive concentration higher than that of pristine SnO_2 (−5.35 mV). A high absolute value of ζ-potential indicates strong electrostatic repulsion between the particles in colloidal solutions, which increases stability.[57] The electrostatic potentials of CsF-5 and CsCl-5 additives are −11.37 and −22.96 mV, respectively, after 7 days, and the original additive decreases to −1.84 mV. CsF and CsCl additives increase the electrostatic potential and antiaggregation similar to commercially available SnO_2 solutions containing the KOH dispersant.[58] The optimized CsCl-SnO_2 and CsF-SnO_2 clusters are well-controlled between 10 and 20 nm and the ideal size for a uniform SnO_2-based ETL.[59] The CsF- and CsCl-modified ETLs show considerably thinner thickness control, probably attributed to the well-controlled agglomeration in the solution. The annealing of SnO_2 films aggregates SnO_2 particles.[60] Thus,

https://doi.org/10.1021/acsomega.4c06621
ACS Omega 2024, 9, 48374−48389

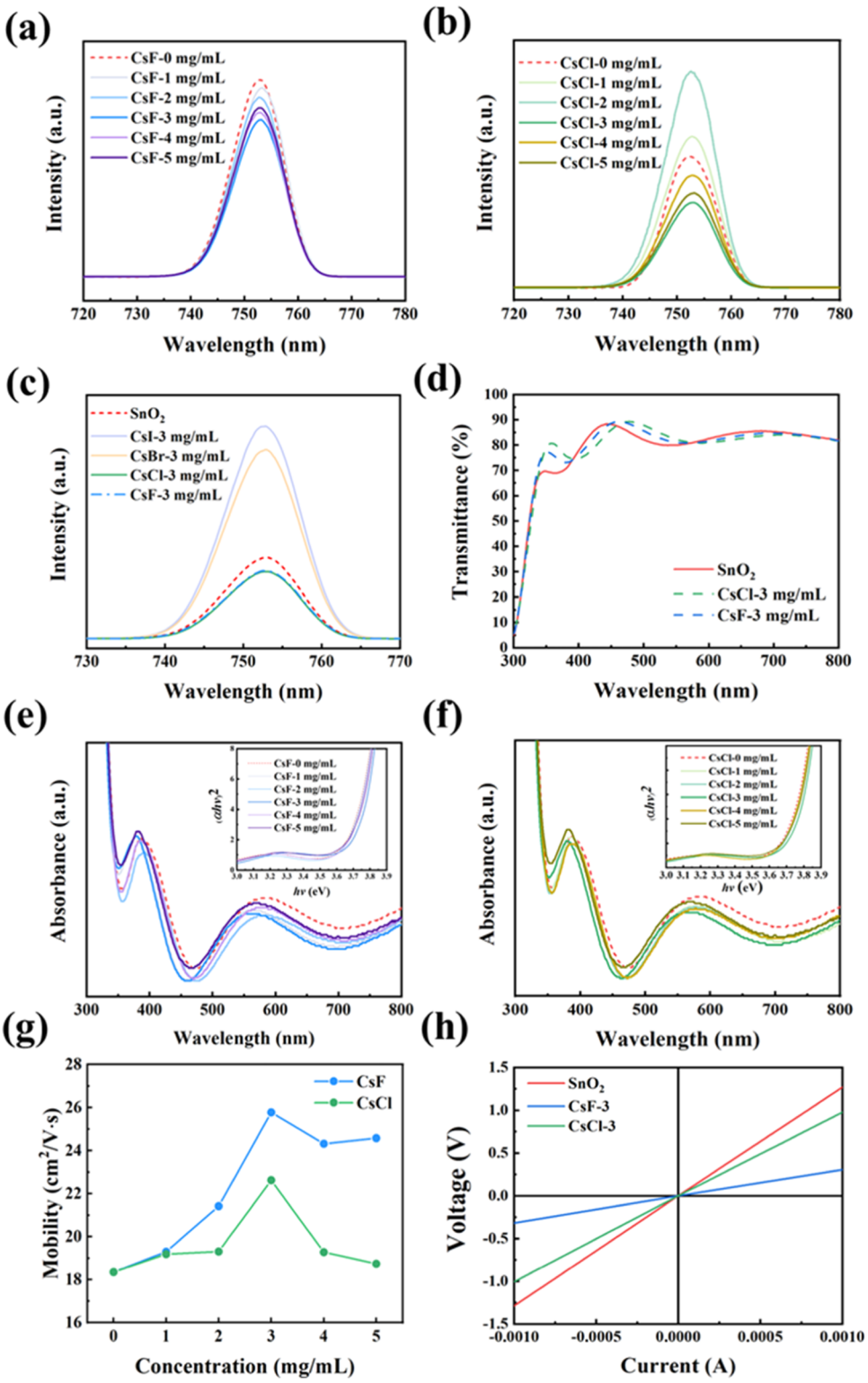

Figure 5. (a, b) PL spectra of the Q-2D perovskite absorber deposited on various ETLs. (c) PL spectra of SnO_2-based ETL based on 3 mg mL^{-1} CsI, CsBr, CsCl, and CsF. (d) Transmittance spectra of the pristine and modified ETLs. UV−vis absorption spectra and corresponding Tauc plots (inset) of ETLs obtained by doping with different (e) CsF and (f) CsCl concentrations. (g) Electron mobility of SnO_2-based ETLs with varying concentrations of CsF and CsCl. (h) *I*−*V* curves of Ag/SnO_2/ITO, Ag/CsF-SnO_2/ITO, and Ag/CsCl-SnO_2/ITO structures via Hall characterization. The doping concentration is 3 mg mL^{-1}.

the uniform doping of CsF and CsCl in a SnO_2-based ETL was verified via energy-dispersive X-ray spectroscopy (EDS). The dispersion of the additives in SnO_2 films after annealing was verified. The EDS results (Figure S12) show that CsF-3 and CsCl-3 have uniformly dispersed Cs^+, F^-, and Cl^- ions, demonstrating that additives can improve the agglomeration of SnO_2 in colloidal dispersion[61] and ions are successfully introduced into SnO_2 films. No large grains (ITO substrate)

https://doi.org/10.1021/acsomega.4c06621
ACS Omega 2024, 9, 48374−48389

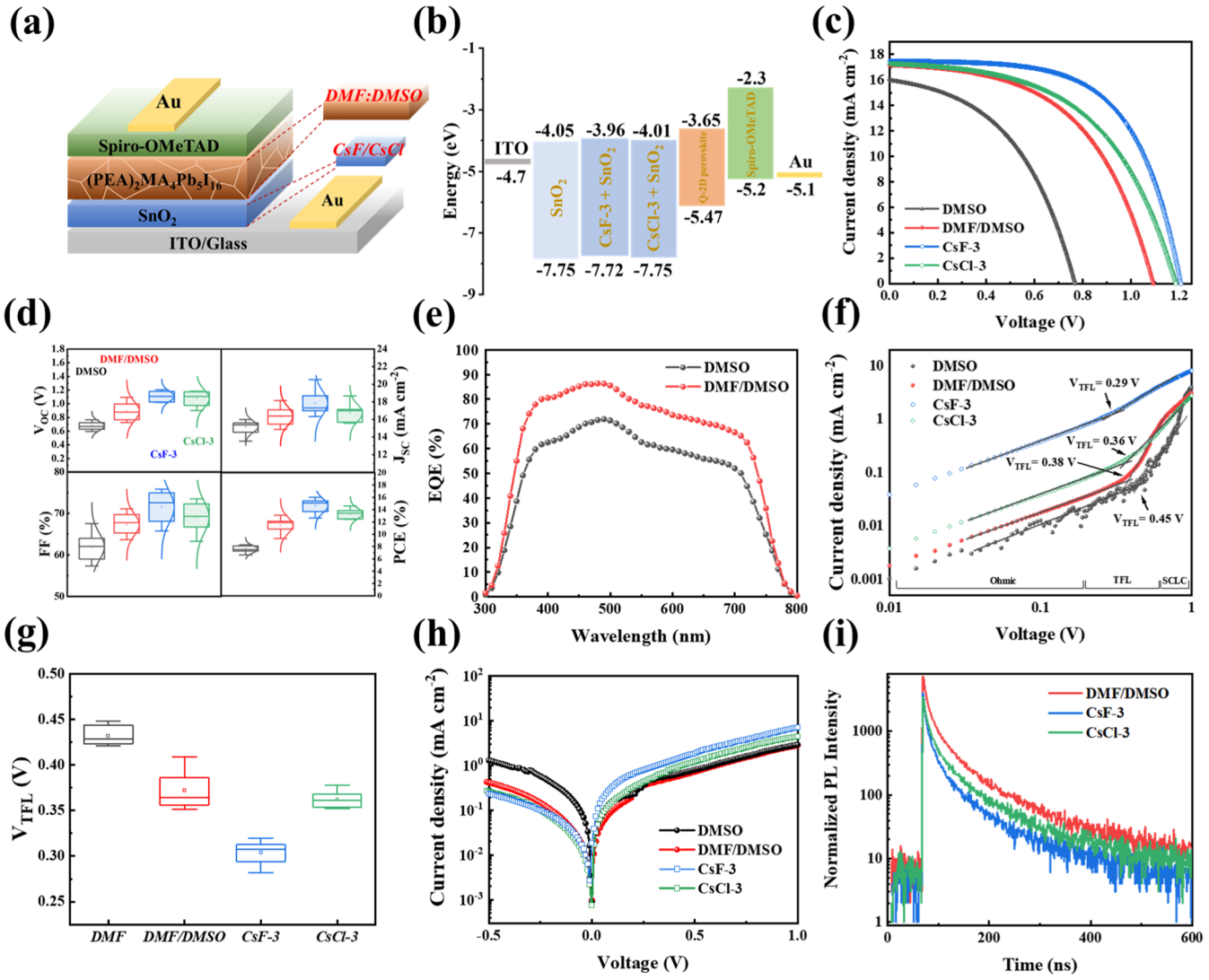

Figure 6. (a) Q-2D PSC structure. (b) Energy band diagram of Q-2D PSCs. (c) $J-V$ curves for the optimized planar PSCs under an AM1.5G solar simulator using Q-2D $(PEA)_2MA_4Pb_5I_{16}$ perovskite films formed using HISs with different solvent ratios and modified ETLs. (d) Statistical distributions of V_{oc}, J_{sc}, FF, and PCE of Q-2D PSCs (data collected from 30 to 40 cells). (e) External quantum efficiency spectra of the devices. (f) Space-charge-limited current (SCLC) curves showing the typical three regions. (g) Statistical distribution of V_{TFL} from SCLC curves (data collected from 10 cells). (h) Dark $J-V$ curves of various Q-2D PSCs. (i) TRPL spectra of Q-2D $(PEA)_2MA_4Pb_5I_{16}$ films deposited on the pristine SnO_2, CsF-3-SnO_2, and CsCl-3-SnO_2 ETLs.

are observed (Figure S8) as the aggregation of SnO_2 particles is effectively prevented by CsCl and CsF during annealing,[57] resulting in the formation of a uniform modified SnO_2-based ETL film.

The dynamics of the electron extraction capacity and recombination of PSCs were investigated by using steady-state PL with different concentrations of CsF and CsCl. Literature reports[53−59] rarely compare the doping of a film with different ion solutions as most reports refer to a single ionic solution. We compared halogen-containing CsBr- and CsI-modified SnO_2 to explore the suitable HIS system for preparing Q-2D perovskite with an appropriate ETL, as shown in Figure 5a−c. No significant shift in the PL peak position indicates that the doping ionic solution maintains consistency in SnO_2 colloidal solutions with an optimal doping concentration of 3 mg mL^{-1}. CsF-3 and CsCl-3 have the lowest PL intensity, indicating better charge transfer properties. The quality of the modified films decreases with an increasing concentration of doped F, which might be owing to the low boiling point of the complex compounds that thermally facilitate ionic diffusion during the growth of CsF-SnO_2 and CsCl-SnO_2 crystals.[53,62] However, the PL intensity as shown in Figure 5c of the optimally modified CsF-SnO_2 and CsCl-SnO_2 ETLs is higher than that of the untreated film, which might be owing to the larger radius of Br^- and I^-, making it difficult for ions to enter the SnO_2 lattice. The transmission spectra in Figure 5d show a high transmittance of the doped films, even higher than that of the pristine SnO_2 film in the short wavelength region beneficial for the fabrication of PSCs before and after introducing CsF and CsCl into the SnO_2-based ETL on the ITO. The high transmittance of the ETL allows more incident light to reach the absorber layer, which improves the light-harvesting efficiency.

The charge carrier dynamics and performance of PSCs have a strong relation with the bulky electrical property of the ETL. The optical bandgap of the ETL directly determines the electron extraction efficiency from the PF. CsF-SnO_2 and CsCl-SnO_2 ETLs show absorption edges at ∼370 nm in the

https://doi.org/10.1021/acsomega.4c06621
ACS Omega 2024, 9, 48374−48389

Table 3. Photovoltaic Performance of Cells

	V_{oc} (V)	J_{sc} (mA cm^{-2})	FF (%)	PCE (%)	J_{sc}[a] (mA cm^{-2})	PCE[b] (%)	avg. PCE (%)
DMSO	0.768	15.99	67.59	8.3	15.86	8.23	8.12 ± 0.31
DMF/DMSO	1.093	17.15	69.83	13.09	17.02	12.99	12.81 ± 0.38
CsF-3	1.206	17.47	76.1	16.02	17.38	15.95	15.83 ± 0.56
CsCl-3	1.185	17.26	71.3	14.58	17.12	14.46	14.11 ± 0.52

[a]Calculated current density derived by integrating the EQE spectrum. [b]PCE corrected by the current density obtained through the EQE spectrum.

UV−vis absorption spectra (Figure 5e,f). The resulting band gaps are summarized in Table S3. The band gaps are slightly wider with an increasing concentration of CsF and CsCl up to 3 mg mL^{-1} owing to the Burstein−Moss effect, which describes the function between the up-shifted Fermi level and increased carrier concentration caused by the filling of states in the conduction band.[63] An increase in CsF and CsCl concentrations narrows the bandgap owing to the many-body interaction effect by F^- and Cl^- with free carriers.[64] The electron mobility depends on grain boundaries and ionized impurity migration based on the scattering mechanism.[65] Figure 5g compares the mobility of the Hall characterization of CsF-3 and CsCl-3 films with different concentrations. The electron mobility of CsF-0 is 18.35 cm^2 V^{-1} s^{-1}. The electron mobility follows a trend similar to that of the carrier concentration and Fermi-level shift as the concentration increases with the high values of 25.78 and 22.63 cm^2 V^{-1} s^{-1} for CsF-3 and CsCl-3, respectively. Table S4 summarized the detailed carrier density (n), electron mobility (μ), and Fermi-level changes (ΔE_f) of all modified SnO_2 films from Hall measurement. Au/SnO_2/ITO device structures were fabricated under various conditions to evaluate their electrical conductivity (Figure 5h). The conductivities (I−V curves) of CsF-SnO_2 and CsCl-SnO_2 ETLs are higher than that of the pristine SnO_2 ETL, indicating that the current density of the modified SnO_2 devices is higher than that of the pristine SnO_2 devices at the same bias voltage, providing an efficient pathway for electron transfer. We compared the Q-2D PMPI morphology deposited on CsF-3-SnO_2 and CsCl-3-SnO_2 ETLs in Figure S13a,b. Dense and continuous Q-2D PFs are formed on both ETLs. The average crystal sizes of the calcite films deposited on CsF-3-SnO_2 (10.32 μm) and CsCl-3-SnO_2 (9.31 μm) are larger than that of the films on unmodified SnO_2, which was 8.39 μm (Figure S13c,d). The micron-level grain growth benefits from the modified ETL,[66] and the improvement of the grain boundaries of the active layer also favors the charge transport in PSCs.

Photovoltaic Characterization and Durability of PSCs. The planar structures of Au/spiro-MeOTAD/Q-2D PMPI/CsF-SnO_2 or CsCl-SnO_2/ITO substrates were considered to investigate the effects of the HIS with different solvent ratios and ETL modifications on the photovoltaic performance (Figure 6a). Based on previous reports, the corresponding flat-band energy levels are shown in Figure 6b.[6,9,28,66] The structure of Au/spiro-MeOTAD/Q-2D PMPI (using DMSO)/SnO_2/ITO substrates is labeled as DMSO; the structure of Au/spiro-MeOTAD/Q-2D PMPI (using DMF/DMSO= 8:2)/SnO_2/ITO substrates is labeled as DMF/DMSO; the structure of Au/spiro-MeOTAD/Q-2D PMPI (using DMF/DMSO= 8:2)/CsF-3 mg mL^{-1}-SnO_2/ITO substrates is labeled as CsF-3; and the structure of Au/spiro-MeOTAD/Q-2D PMPI (using DMF/DMSO= 8:2)/CsCl-3 mg mL^{-1}-SnO_2/ITO substrates is labeled as CsCl-3. The champion performance photocurrent density−voltage (J−V) characteristic curves of PEA-based Q-2D PSCs were measured under standard AM1.5G illumination (100 mW cm^{-2}) (Figure 6c). The corresponding photovoltaic parameters are summarized in Table 3. The PSC prepared from the DMSO-based Q-2D PMPI has the following parameter values: short-circuit current (J_{sc}) = 15.99 mA cm^{-2}, open-circuit voltage (V_{oc}) = 0.768 V, fill factor (FF) = 0.6759, and PCE = 8.28%. The PCE of PSCs prepared in the HIS increased from 8.28 to 13.09%, an improvement of >55%. The increase in efficiency is mainly attributed to the enhancement of V_{oc} and J_{sc}, which is consistent with the observed improvement in film quality and photovoltaic properties. We collected data from 30 to 40 devices for each PEA-based sample (Figure 6d) and observed a statistically significant improvement in the device performance after the addition of DMSO to the first priming layer in the HIS: the average V_{oc} increased from 0.689 to 0.903 V, FF from 63.7 to 67.2%, J_{sc} from 15.76 to 16.89 mA cm^{-2}, and PCE from 7.89 to 11.82% with an average PCE improvement of 49%. The improved photovoltaic performance of PEA-based Q-2D PSCs can be attributed to the improved quality of the Q-2D PMPI film owing to the first priming layer-controlled crystal growth method, such as the increased grain size and improved crystal orientation.[8,11]

Introducing CsF and CsCl via annealing at ultralow temperature into the SnO_2-based ETL exhibits better photovoltaic performance than that of the unmodified SnO_2-based PSCs. The PSCs of CsF-3 and CsCl-3 show the best performance with the highest PCE of 16.02 and 14.58%, respectively. The CsF-3-SnO_2-based PSC has a V_{oc} of 1.206 V, J_{sc} of 17.47 mA cm^{-2}, FF of 76.1%, and PCE of 16.02%, which can be attributed to the improved electron extraction efficiency. By contrast, the CsCl-3-SnO_2-based PSC exhibits poorer performance than the CsF-3-SnO_2-PSC owing to the poor electronic properties of CsCl-SnO_2. This shows the relation between photocurrent and the Fermi level of the ETL. The up-shifted Fermi level with the introduction of CsF and CsCl can decrease the energy band offset between the ETL and active layer, inducing an increasing V_{oc}.[67] The high electron extraction efficiency of CsF-SnO_2 and CsCl-SnO_2 is attributed to the enlarged J_{sc}.

External quantum efficiency was measured to study the nature of the J_{sc} enhancement in the DMF/DMSO-based PSC, as shown in Figure 6e. The spectral response of the DMF/DMSO-based PSC with the grain structure is higher than that of the DMSO-based PSC, suggesting that the PSC has a high photon-to-electron conversion efficiency. This improvement is related to optimizing the Q-2D PMPI crystal orientation, which efficiently converts to charge carriers and is collected by the terminal electrode. Notably, Q-2D PFs have a low external quantum efficiency in the long wavelength region. This result is consistent with the UV−vis absorption spectrum in Figure 4a.

The SCLC technique was used to investigate the changes in the electron trap density of the PSC after structural optimization and the ETL modification of Au/Q-2D packaged

https://doi.org/10.1021/acsomega.4c06621
ACS Omega 2024, 9, 48374−48389

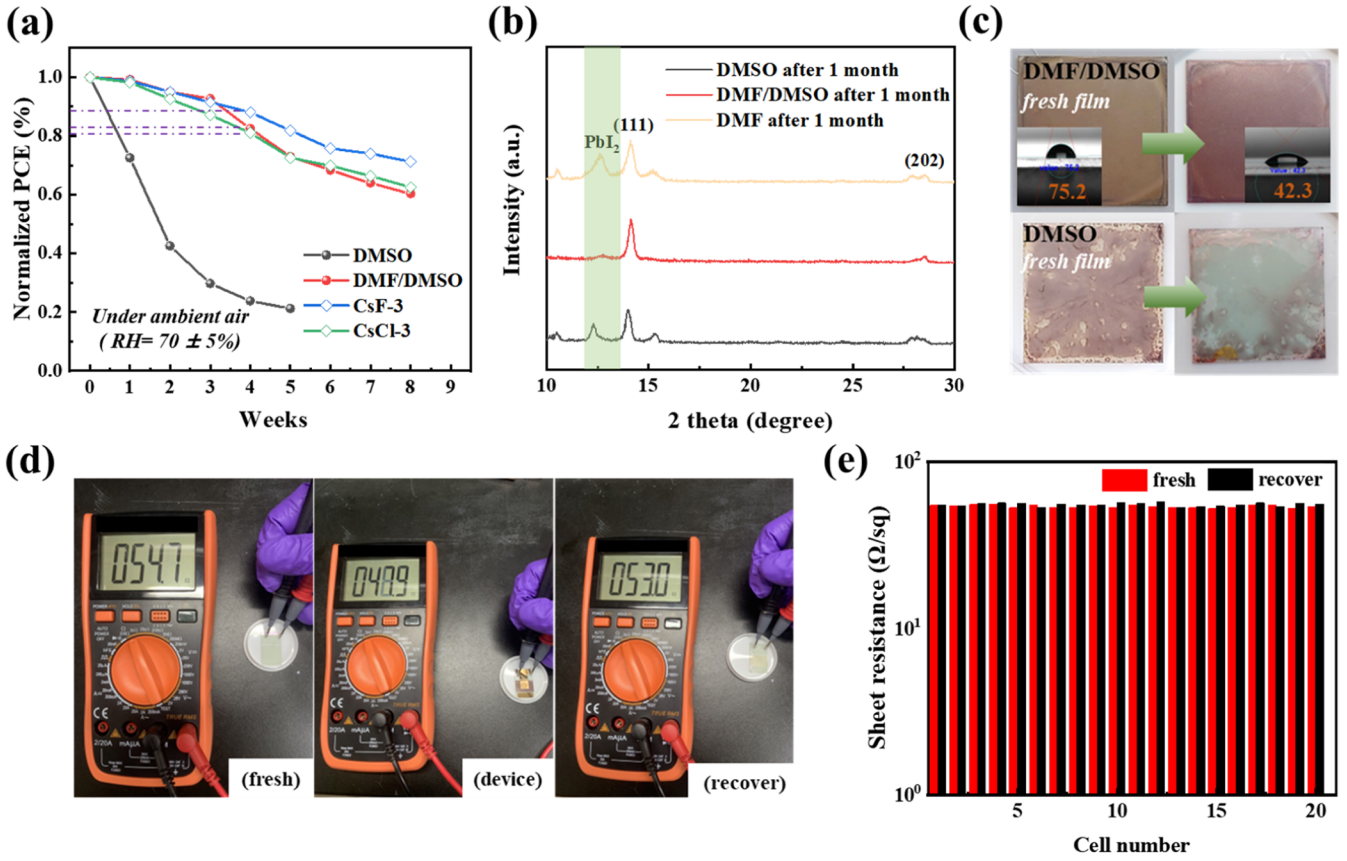

Figure 7. (a) Normalized PCE and long-term stability of unencapsulated Q-2D PSCs after 8 weeks of aging in the air with >65% relative humidity. (b) GIXRD patterns and (c) optical imaging of unencapsulated Q-2D $(PEA)_2MA_4Pb_5I_{16}$ films after storage in the air for 1 month with >65% relative humidity (inset shows contact angle measurements). (d) Resistance measurement of fresh and recovered ITO/glass substrates. (e) Substrate-to-substrate variation of the fresh and recovered sheet resistances for 20 different substrates.

crystal/ETL/ITO structured devices, as shown in Figure 6f. The $J-V$ curves change from the low-voltage linear region (ohmic region) to the trap-filling limit region and finally reach the SCLC region.[68] N_{trap} is evaluated by the starting voltage in the trap-filling limit (TFL) region (V_{TFL}). Carrier mobility is derived from the SCLC region. The trap density (N_{trap}) is calculated using eq 1[69]

$$N_{trap} = (2\varepsilon_0\varepsilon_r V_{TFL})/(eL^2) \quad (1)$$

where N_{trap} is the trap density, ε_r is the relative dielectric constant,[70] ε_0 is the vacuum permittivity (8.85×10^{-12} F m^{-1}),[69] e and L are the elementary charge and thickness of the PF, respectively.[71] The increased current in the TFL region can be attributed to the continuously filled trap states until they reach the trap-filled limit voltage (V_{TFL}). The electron trap density of the DMF/DMSO-based PSC (V_{TFL} = 0.38 V) active layer is lower than the DMSO-based PSC (V_{TFL} = 0.45 V) with calculated electron trap densities of states of 7.42×10^{15} and 6.26×10^{15} cm^{-3}, respectively. HIS-based Q-2D PFs considerably reduce the defects in the active layer by improving the lattice orientation to suppress trap-assisted nonradiative recombination. The results correspond to films with large grain sizes and low PL intensities of Q-2D perovskites (Figures 3a and 4b). The reduction in V_{TFL} indicates that the Q-2D perovskite trap density is reduced by the doping of CsF on SnO_2. Introducing CsF and CsCl into the ETL significantly decreases defect density to 4.78×10^{15} and 5.93×10^{15} cm^{-3}, respectively, compared to devices based on the unmodified ETL. Alternately, the CsF-based device has the lowest V_{TFL} (0.29 V). Figure 6g shows that the average V_{TFL} measurements for 10 samples are consistent with the results presented in Figure 6f, demonstrating the repeatability of the grain structure of the PSCs. The lower trap density improves the electron transfer efficiency, which enhances the PCE in PSCs. This agrees with SCLC results, indicating that doping CsF or CsCl reduces the defects of the ETL and PFs.

Analyzing the different optoelectronic properties indicates the internal characteristics of the PSC device. The dark $J-V$ curves in Figure 6h demonstrate the $J-V$ characteristics of a PSC measured in the dark. Optimized PSC with a lower dark current and higher photocurrent. All optimized devices show low dark J_{sc}, indicating low bulk defects in the Q-2D perovskite layer,[72] suppressing charge recombination and optimizing charge extraction. The optimized device produces a high V_{oc} owing to leakage current suppression.[73] CsF has the highest V_{oc} (1.206 V), as the additives cause the passivation of perovskites and the ETL interfaces. Thus, the defect-induced carrier generation rate is reduced, resulting in the lowest leakage currents.[66] CsF- and CsCl-modified ETLs can effectively mitigate defects in PFs and reduce the current shunt paths.

Charge recombination in PSCs was analyzed via time-resolved photoluminescence (TRPL) decay spectra to determine the recombination kinetics of Q-2D PMPI/ETL/ITO structures, as shown in Figure 6i. The fast decay (τ_1) lifetime is attributed to the charge extraction from the ETL,

https://doi.org/10.1021/acsomega.4c06621
ACS Omega 2024, 9, 48374−48389

while the slow decay (τ_2) is attributed to the recombination process inside the PF.[74] The excitation light incident on one side of the ITO substrate measures the τ_1 and τ_2 atoms of Q-2D PF deposited on unmodified SnO_2 as 35.2 and 186.2 ns, respectively. CsF- and CsCl-incorporated SnO_2 layers have shortened τ_1 of 10.8 and 12.3 ns, respectively. The average carrier lifetime is reduced by 30%, confirming that the modification improves the extraction and transport of photogenerated electrons and reduces the defect density. The carrier lifetimes of CsF-3 and CsCl-3 are shorter than those of unmodified SnO_2 attributed to the formation of strong Pb−Cl and Pb−F bonds on the surface and the passivation of the trap density at the interface, which facilitates the extraction of charge carriers.

The long-term stability of Q-2D PMPI PFs and PSC devices was investigated simultaneously. All PSCs were stored in the air with a high RH of 70 ± 5%, in darkroom and room temperature (25 °C) conditions, and aged for 8 weeks (Figure 7a). The optimized DMF/DMSO-based devices maintained ∼80−86% of their original PCE after storage in the air for 1 month (720 h). The PCE was maintained in the range 58−71% after 2 months, exhibiting excellent stability in humid conditions. Alternately, the PCE of the DMSO-based PSC device reduces to 22% after 1 min under the same storage condition. Table S5 shows earlier reports of PSCs based on various PEAI-based Q-2D perovskite materials of different systems with good PCE and long-term stability. We have improved the crystal structure of the Q-2D PMPI PF using the HIS, which hinders the reduction of the PF in moisture and allows for structural optimization before adding additives (or ionic doping) to the Q-2D absorber layer, resulting in excellent device durability. The PSC with an ion-modified ETL has excellent properties. CsF-3- and CsCl-3-based PSCs have slightly better durability than the DMF/DMSO-ETL-based PSC. Earlier reports indicate that the modification of the ETL can passivate surface defects and slow down the degradation of PCE,[54] similar to our results. However, in this study, we consider the optimized first priming layer in the optimized structure for mitigating the degradation of the film affecting the PCE.

The GIXRD pattern and optical images of Q-2D PMPI show that DMF- and DMSO-based films stored under conditions similar to those of the PSC for 1 month (Figure 7b,c) have PbI_2 peaks at 12.6°, indicating the rapid decomposition of unoptimized PFs. However, no noticeable material degradation is observed for the optimized DMF/DMSO-based PF with only a slight decrease in the GIXRD intensity, demonstrating its durability for storing in the atmosphere. Although Spiro-OMeTAD is a common HTL, the deterioration of HTL changes the PSC efficiency (Figure S14). The HTL was oxidized after 1 month under the same conditions, proving that the commercialization of PSCs requires the optimization of each layer.[75] The synthesized Q-2D PSCs enable the recycling and reuse of ITO/glass substrates after cleaning with acetone or ultrasonic cleaners, reducing carbon emissions (net-zero strategy). Figure 7d,e shows a similar resistance of ITO substrates before and after cleaning of 20 cells. Thus, an HIS process approach is reported in this study that tunes the morphology of the first priming layer under high humidity while ionically modifying the ETL for passivation of defects at the bulk and layer interfaces. This affects the vertical growth and phase distribution of Q-2D PFs, which optimizes the performance of PSCs and drastically improves the durability of the PSCs in the air. This effective strategy can be applied to relevant perovskite devices such as memories, light-emitting diodes, and photodetectors. The devices are fabricated and stored in low energy-consuming devices compliant with the Paris Agreement[31] and CBAM.[32] The highly stable structure will promote commercialization of PSCs in the future.

CONCLUSIONS

We have demonstrated a novel intermediate-controlled crystal growth method for synthesizing Q-2D PMPI perovskite. In the first step, the first priming layer was grown in a preferred orientation perpendicular to the substrate by appropriately adjusting the ratio of the HIS (DMF:DMSO = 8:2) with 100% substrate coverage, which greatly influenced the formation of the final Q-2D PF. The (111)-optimally oriented microstructure forms ordered, highly crystalline PFs with excellent charge transport, suppressed nonradiative recombination, and moisture-resistant capability. An appropriate adjustment of the coordination of the solvent and Q-2D compounds can effectively transform disordered grains and phase distribution into ideal grains with the micron-level grain size grown perpendicular to the substrate with relatively pure and homogeneously distributed phases. The HIS system increased the PCE of Q-2D PSCs by >55% reaching to 13.09%. Ion-modified ETLs synthesized at an ultralow temperature also increased the PCE to 16.02% without destroying the HIS system. The HIS-based first priming layer can be essential in commercializing Q-2D perovskite for highly efficient and reproducible perovskites with long-term stability (88% PCE maintained for 1 month) in other photovoltaic applications. Unpackaged PSCs, ETLs, and HTLs reduced power consumption, making the HIS Q-2D perovskite system more compatible with the future solar industry with carbon emission management.

ASSOCIATED CONTENT

Supporting Information

The Supporting Information is available free of charge at https://pubs.acs.org/doi/10.1021/acsomega.4c06621.

FWHM of Figure S5e of Q-2D $(PEA)_2MA_4Pb_5I_{16}$ films (Table S1); ζ-potential and average colloidal diameter for fresh and aged colloidal solutions of SnO_2 with 1, 3, or 5 mg mL^{-1} of CsF and CsCl via DLS (Table S2); band gaps (E_g) of 0, 1, 2, 3, 4, or 5 mg mL^{-1} of CsF-SnO_2 and CsCl-SnO_2 ETLs calculated from Tauc plots (Table S3); electrical properties of pristine and different concentrations of materials doped with ion-modified ETL of 0, 1, 2, 3, 4, or 5 mg mL^{-1} of CsF-SnO_2 and CsCl-SnO_2 (Table S4); comparison of Au/Spiro-MeTAD/$(PEA)_2(MA)_4Pb_5I_{16}$/ETL/ITO prepared using the HIS via a two-step method with previously reported PEAI-Based Q-2D PSCs (Table S5); (a) comparison of PbI_2/PEAI precursor dissolution speed in pure DMF and DMSO at room temperature and (b) optical images of the first priming layer crystals grown on a hot plate at 70 °C at different immersion durations in pure DMF and DMSO (Figure S1); (a) optical images of the first priming layer obtained according to different immersion times and DMF/DMSO ratios (after annealing for 10 min on a 70 °C hot plate) and (b) calculated substrate coverage of the first priming

https://doi.org/10.1021/acsomega.4c06621
ACS Omega 2024, 9, 48374−48389

layer (first step) (Figure S2); (a) SEM image at different magnifications of the first priming layer of the nanoplates with a nanoporous surface obtained in the first step (DMF/DMSO = 8:2), (b) UV−vis spectra and (c) XRD pattern of the first priming layer obtained from the first step using HISs with different solvent ratios (Figure S3); Q-2D $(PEA)_2MA_4Pb_5I_{16}$ film grain size distribution analysis prepared using (a) HIS and (b) DMSO-based first priming layers (MAI dropping amount of 110 μL) and (c) corresponding Tauc plot of Q-2D $(PEA)_2MA_4Pb_5I_{16}$ films based on HISs with different solvent ratios (Figure S4); (a−d) top views of SEM images of the standard Q-2D structure, (e) XRD pattern and (f) PL spectra of square-shaped grains of Q-2D $(PEA)_2MA_4Pb_5I_{16}$ films with different MAI dropped amounts in the second step (Figure S5); SEM images of Q-2D $(PEA)_2MA_4Pb_5I_{16}$ fabricated in different relative humidities in the second step: (a) 30 ± 5%, (b) 40 ± 5%, (c) 50 ± 5%, and (d) 60 ± 5% RHs (Figure S6); XPS spectra of (a) I 3d, (b) C 1s, and (c) Pb 4f of Q-2D $(PEA)_2MA_4Pb_5I_{16}$ (Figure S7); SEM top-view image of SnO_2-based ETLs with (a) CsF-0, (b) CsF-3, (c) CsF-5, (d) CsCl-3, and (e) CsCl-5 mg mL^{-1}, inset shows contact angle measurement, and (f) average grain size of various ETLs (Figure S8); SEM cross-section images and thickness of SnO_2-based ETLs modified with different ionic solutions: (a) pristine SnO_2, (b) CsF-3, (c) CsF-5, (d) CsCl-3, and (e) CsCl-5 mg mL^{-1} (Figure S9); DLS number-average distributions and cumulative proportion of different sizes of SnO_2 particles in (a) 0, (b) 1, (c) 3, and (d) 5 mg mL^{-1} of the CsF solution (Figure S10); ζ-potential of (a) SnO_2, (b) CsF-5, and (c) CsCl-5 mg mL^{-1} doping concentrations (Figure S11); elemental mapping of EDS of (a) CsF-3- and (b) CsCl-3-modified ETLs (Figure S12); (a, b) SEM morphology and (c, d) grain size distribution analysis of Q-2D $(PEA)_2MA_4Pb_5I_{16}$ films deposited on CsF-SnO_2 and CsCl-SnO_2 ETLs (Figure S13); and optical images of HTL after aging in the air after 1 month (Figure S14) (PDF).

AUTHOR INFORMATION

Corresponding Author

Fu-Hsiang Ko − *Department of Materials Science and Engineering, National Yang Ming Chiao Tung University, Hsinchu 30010, Taiwan;* orcid.org/0000-0001-6464-1737; Email: fhko@nycu.edu.tw

Authors

Yen-Shuo Chen − *Department of Materials Science and Engineering, National Yang Ming Chiao Tung University, Hsinchu 30010, Taiwan*

Min-Han Hsieh − *Department of Materials Science and Engineering, National Yang Ming Chiao Tung University, Hsinchu 30010, Taiwan*

Ching-Chang Lin − *Department of General Systems Studies, Graduate School of Arts and Sciences, The University of Tokyo, Tokyo 153-8902, Japan;* orcid.org/0000-0003-0970-3071

Yi-Cheng Huang − *Department of Materials Science and Engineering, National Yang Ming Chiao Tung University, Hsinchu 30010, Taiwan*

Shang-Yu Tsai − *Department of Materials Science and Engineering, National Yang Ming Chiao Tung University, Hsinchu 30010, Taiwan*

Complete contact information is available at: https://pubs.acs.org/10.1021/acsomega.4c06621

Notes

The authors declare no competing financial interest.

ACKNOWLEDGMENTS

The authors are grateful to the National Science and Technology Council of Taiwan for financially supporting this research under Contracts NSTC 113-2113-M-A49-012, NSTC 112-2119-M-002-032-MBK, and NSTC 113-2119-M-492-004-MBK. This work was supported by the Higher Education Sprout Project of the National Yang Ming Chiao Tung University and Ministry of Education (MOE), Taiwan. The authors also thank the Taiwan Semiconductor Research Institute (TSRI), Hsinchu, for the device processing and characterization supported.

ABBREVIATIONS

AFM, atomic-force microscopy; DLS, dynamic light scattering; EDS, energy-dispersive X-ray spectroscopy; ETL, electron transport layer; FF, fill factor; GIXRD, grazing incidence X-ray diffraction; HIS, hybrid immersion solvent; HTL, hole transport layer; ITO, indium titanium oxide; PCE, power conversion efficiency; PF, perovskite films; PSC, perovskite solar cell; RH, relative humidity; RMS, root-mean square; SEM, scanning electron microscopy; TFL, trap-filling limit; XPS, X-ray photoelectron spectroscopy; AM, air mass; Q-2D, quasi-two-dimensional; 3D, three-dimensional; TRPL, time-resolved photoluminescence; BA^+, butylammonium; PEA^+, phenylethylammonium; MA^+, methylammonium; FA^+, formamidinium; DMSO, dimethyl sulfoxide; PEAI, phenethylammonium iodide; CBAM, carbon border adjustment mechanism; DMF, *N*,*N*-dimethylformamide; PMPI, $(PEA)_2MA_4Pb_5I_{16}$; CsF, cesium fluoride; CsCl, cesium chloride; CsBr, cesium bromide; CsI, cesium iodide; MAI, methylammonium iodide; TBP, tributyl phosphate; TFSI, Li-bis(trifluoromethylsulfonyl)imide; FWHM, full width at half-maximum; PL, photoluminescence; UV−vis, ultraviolet−visible; J_{sc}, short-circuit current; V_{oc}, open-circuit voltage; N_{trap}, trap density; V_{TFL}, trap density; ε_r, relative dielectric constant; ε_0, vacuum permittivity; SCLC, space-charge limited current; τ_1, fast decay; τ_2, slow decay

REFERENCES

(1) Zhang, Y.; Park, N. Quasi-Two-Dimensional Perovskite Solar Cells with Efficiency Exceeding 22%. *ACS Energy Lett.* **2022**, 7 (2), 757−765.

(2) Li, K.; Gan, X.; Zheng, R.; Zhang, H.; Xiang, M.; Dai, S.; Du, D.; Zhang, F.; Guo, L.; Liu, H. Comparative Analysis of Thiophene-Based Interlayer Cations for Enhanced Performance in 2D Ruddlesden-Popper Perovskite Solar Cells. *ACS Appl. Mater. Interfaces* **2024**, *16* (6), 7161−7170.

(3) Bai, J.; Wang, H. J.; Ma, J.; Zhao, Y.; Lu, H.; Zhang, Y.; Gull, S.; Qiao, T.; Qin, W.; Chen, Y.; Jiang, L.; Long, G.; Wu, Y. Wafer-Scale Patterning Integration of Chiral 3D Perovskite Single Crystals toward High-Performance Full-Stokes Polarimeter. *J. Am. Chem. Soc.* **2024**, *146*, 18771−18780.

(4) Lai, X.; Li, W.; Gu, X.; Chen, H.; Zhang, Y.; Li, G.; Zhang, R.; Fan, D.; He, F.; Zheng; Yu, J.; Chen, R.; Kyaw, A. K. K.; Sun, X. W. High-Performance Quasi-2D Perovskite Solar Cells with Power

Conversion Efficiency Over 20% Fabricated in Humidity-Controlled Ambient Air. *Chem. Eng. J.* **2022**, *427*, No. 130949.
(5) Yu, S.; Yan, Y.; Chen, Y.; Chábera, P.; Zheng, K.; Liang, Z. Enabling Room-Temperature Processed Highly Efficient and Stable 2D Ruddlesden-Popper Perovskite Solar Cells with Eliminated Hysteresis by Synergistic Exploitation of Additives and Solvents. *J. Mater. Chem. A* **2019**, *7*, 2015−2021.
(6) Fu, W.; Liu, H.; Shi, X.; Zuo, L.; Li, X.; Jen, A. K. Y. Tailoring the Functionality of Organic Spacer Cations for Efficient and Stable Quasi-2D Perovskite Solar Cells. *Adv. Funct. Mater.* **2019**, *29*, No. 1900221.
(7) Zhang, Y.; Chen, M.; He, T.; Chen, H.; Zhang, Z.; Wang, H.; Lu, H.; Ling, Q.; Hu, Z.; Liu, Y.; Chen, Y.; Long, G. Highly Efficient and Stable FA-Based Quasi-2D Ruddlesden-Popper Perovskite Solar Cells by the Incorporation of β-Fluorophenylethanamine Cations. *Adv. Mater.* **2023**, *35*, No. 2210836.
(8) Wang, Z.; Wei, Q.; Liu, X.; Liu, L.; Tang, X.; Guo, J.; Ren, S.; Xing, G.; Zhao, D.; Zheng, Y. Spacer Cation Tuning Enables Vertically Oriented and Graded Quasi-2D Perovskites for Efficient Solar Cells. *Adv. Funct. Mater.* **2021**, *31*, No. 2008404.
(9) (a) Li, X.; Wu, G.; Wang, M.; Yu, B.; Zhou, J.; Wang, B.; Zhang, X.; Xia, H.; Yue, S.; Wang, K.; Zhang, C.; Zhang, J.; Zhou, H.; Zhang, Y. Water-Assisted Crystal Growth in Quasi-2D Perovskites with Enhanced Charge Transport and Photovoltaic Performance. *Adv. Energy Mater.* **2020**, *10*, No. 2001832. (b) Qing, J.; Liu, X. K.; Li, M.; Liu, F.; Yuan, Z.; Tiukalova, E.; Yan, Z.; Duchamp, M.; Chen, S.; Wang, Y.; Bai, S.; Liu, M. J.; Snaith, H. J.; Lee, C. S.; Sum, T. C.; Gao, F. Aligned and Graded Type-II Ruddlesden−Popper Perovskite Films for Efficient Solar Cells. *Adv. Energy Mater.* **2018**, *8*, No. 1800185.
(10) Li, K.; Yue, S.; Li, X.; Ahmad, N.; Cheng, Q.; Wang, B.; Zhang, X.; Li, S.; Li, Y.; Huang, G.; Kang, H.; Yue, T.; Zafar, S. U.; Zhou, H.; Zhu, L.; Zhang, Y. High Efficiency Perovskite Solar Cells Employing Quasi-2D Ruddlesden-Popper/Dion-Jacobson Heterojunctions. *Adv. Funct. Mater.* **2022**, *32*, No. 2200024.
(11) Cao, D. H.; Stoumpos, C. C.; Farha, O. K.; Hupp, J. T.; Kanatzidis, M. G. 2D Homologous Perovskites as Light-Absorbing Materials for Solar Cell Applications. *J. Am. Chem. Soc.* **2015**, *137* (24), 7843−7850.
(12) Stoumpos, C. C.; Cao, D. H.; Clark, D. J.; Young, J.; Rondinelli, J. M.; Jang, J. I.; Hupp, J. T.; Kanatzidis, M. G. Ruddlesden-Popper Hybrid Lead Iodide Perovskite 2D Homologous Semiconductors. *Chem. Mater.* **2016**, *28* (8), 2852−2867.
(13) Liang, C.; Gu, H.; Xia, Y.; Wang, Z.; Liu, X.; Xia, J.; Zuo, S.; Hu, Y.; Gao, X.; Hui, W.; Chao, L.; Niu, T.; Fang, M.; Lu, H.; Dong, H.; Yu, H.; Chen, S.; Ran, X.; Song, L.; Li, B.; Zhang, J.; Peng, Y.; Shao, G.; Wang, J.; Chen, Y.; Xing, G.; Huang, W. Two-Dimensional Ruddlesden-Popper Layered Perovskite Solar Cells Based on Phase-Pure Thin Films. *Nat. Energy* **2021**, *6*, 38−45.
(14) Shi, J.; Gao, Y.; Gao, X.; Zhang, Y.; Zhang, J.; Jing, X.; Shao, M. Fluorinated Low-Dimensional Ruddlesden-Popper Perovskite Solar Cells with over 17% Power Conversion Efficiency and Improved Stability. *Adv. Mater.* **2019**, *31*, No. 1901673.
(15) Tsai, H.; Nie, W.; Blancon, J. C.; Stoumpos, C. C.; Asadpour, R.; Harutyunyan, B.; Neukirch, A. J.; Verduzco, R.; Crochet, J. J.; Tretiak, S.; Pedesseau, L.; et al. High-Efficiency Two-Dimensional Ruddlesden-Popper Perovskite Solar Cells. *Nature* **2016**, *536*, 312−316.
(16) Yang, W.; Zhan, Y.; Yang, F.; Li, Y. Hot-Casting and Antisolvent Free Fabrication of Efficient and Stable Two-Dimensional Ruddlesden-Popper Perovskite Solar Cells. *ACS Appl. Mater. Interfaces* **2021**, *13* (51), 61039−61046.
(17) Zhang, X.; Wu, G.; Fu, W.; Qin, M.; Yang, W.; Yan, J.; Zhang, Z.; Lu, X.; Chen, H. Orientation Regulation of Phenylethylammonium Cation Based 2D Perovskite Solar Cell with Efficiency Higher than 11%. *Adv. Energy Mater.* **2018**, *8*, No. 1702498.
(18) Deng, L.; Yang, H.; Liu, Z.; Yang, X.; Huang, Z.; Yu, H.; Wang, K.; Li, J. Effective Phase Control for High-Performance Red-Light-Emitting Quasi-2D Perovskite Solar Cells via MACl Additive. *ACS Appl. Energy Mater.* **2021**, *4* (3), 2856−2863.
(19) Gao, L.; Zhang, F.; Xiao, C.; Chen, X.; Larson, B. W.; Berry, J. J.; Zhu, K. Improving Charge Transport via Intermediate-Controlled Crystal Growth in 2D Perovskite Solar Cells. *Adv. Funct. Mater.* **2019**, *29*, No. 1901652.
(20) Fu, W.; Wang, J.; Zuo, L.; Gao, K.; Liu, F.; Ginger, D. S.; Jen, A. K. Y. Two-Dimensional Perovskite Solar Cells with 14.1% Power Conversion Efficiency and 0.68% External Radiative Efficiency. *ACS Energy Lett.* **2018**, *3* (9), 2086−2093.
(21) Yu, X.; Lv, Y.; Xue, B.; Wang, L.; Hu, W.; Liu, X.; Yang, S.; Zhang, W. H. Multiple Bonding Effects of 1-Methanesulfonyl-Piperazine on the Two-Step Processed Perovskite Toward Efficient and Stable Solar Cells. *Nano Energy* **2022**, *93*, No. 106856.
(22) Lai, H.; Kan, B.; Liu, T.; Zheng, N.; Xie, Z.; Zhou, T.; Wan, X.; Zhang, X.; Liu, Y.; Chen, Y. Two-Dimensional Ruddlesden-Popper, 2 D. Perovskite with Nanorod-Like Morphology for Solar Cells with Efficiency Exceeding 15%. *J. Am. Chem. Soc.* **2018**, *140* (37), 11639−11646.
(23) Li, X.; Li, K.; Wang, B.; Zhang, X.; Yue, S.; Li, Y.; Chen, Q.; Li, S.; Yue, T.; Zhou, H.; Zhang, Y. Efficient and Stable Quasi-2D Perovskite Solar Cells Enabled by Thermal-Aged Precursor Solution. *Adv. Funct. Mater.* **2021**, *31*, No. 2107675.
(24) Yue, T.; Li, K.; Li, X.; Ahmad, N.; Kang, H.; Cheng, Q.; Zhang, Y.; Yue, Y.; Jing, Y.; Wang, B.; Li, S.; Chen, J.; Huang, G.; Li, Y.; Fu, Z.; Wu, T.; Zafar, S. U.; Zhu, L.; Zhou, H.; Zhang, Y. A Binary Solution Strategy Enables High-Efficiency Quasi-2D Perovskite Solar Cells with Excellent Thermal Stability. *ACS Nano* **2023**, *17* (15), 14632−14643.
(25) He, J.; Sheng, W.; Yang, J.; Zhong, Y.; Su, Y.; Tan, L.; Chen, Y. Omnidirectional Diffusion of Organic Amine Salts Assisted by Ordered Arrays in Porous Lead Iodide for Two-Step Deposited Large-Area Perovskite Solar Cells. *Energy Environ. Sci.* **2023**, *16*, 629−640.
(26) Abdy, H.; Heydari, Z.; Aletayeb, A.; Kolahdouz, M.; Asl-Soleimani, E. Electrodeposition, Solvent Engineering, and Two-Step Solution Deposition of the Perovskite Films: Morphological and Structural Study. *J. Mater. Sci. Mater. Electron.* **2021**, *32*, 12991−12999.
(27) Tai, Q.; You, P.; Sang, H.; Liu, Z.; Hu, C.; Chan, H. L. W.; Yan, F. Efficient and stable perovskite solar cells prepared in ambient air irrespective of the humidity. *Nat. Commun.* **2016**, *7*, No. 11105.
(28) Ke, L.; Gan, X.; Zhao, W.; Guo, L.; Liu, H. $(C_6H_5C_2H_4NH_3)_2FA_{n-1}Pb_nI_{3n+1}$: A Quasi-Two-Dimensional Perovskite with High Performance Produced via Two-Step Solution Method. *J. Alloys Compd.* **2019**, *788*, 954−960.
(29) Lu, J.; Yang, T. H.; Niu, T. Q.; Bu, N.; Zhang, Y. L.; Wang, S. Q.; Fang, J. J.; Chang, X. M.; Luo, T.; Wen, J.; Yang, Y.; Ding, Z.; Zhao, K.; Liu. Formamidinium-Based Ruddlesden-Popper Perovskite Films Fabricated via Two-Step Sequential Deposition: Quantum-Well Formation, Physical Properties and Film-Based Solar Cells. *Energy Environ. Sci.* **2022**, *15*, 1144−1155.
(30) Wu, Y.; Islam, A.; Yang, X.; Qin, C.; Liu, J.; Zhang, K.; Peng, W.; Han, L. Retarding the Crystallization of PbI_2 for Highly Reproducible Planar-Structured Perovskite Solar Cells via Sequential Deposition. *Energy Environ. Sci.* **2014**, *7*, 2934−2938.
(31) Fankhauser, S.; Smith, S. M.; Allen, M.; Axelsson, K.; Hale, T.; Hepburn, C.; Kendall, J. M.; Khosla, R.; Lezaun, J.; Mitchell-Larson, E.; Obersteiner, M.; Rajamani, L.; Rickaby, R.; Seddon, N.; Wetzer, T. The Meaning of Net Zero and How to Get It Right. *Nat. Clim. Change* **2022**, *12*, 15−21.
(32) Bellora, C.; Fontagné, L. EU in Search of a Carbon Border Adjustment Mechanism. *Energy Econ.* **2023**, *123*, No. 106673.
(33) Davis, S. J.; Lewis, N. S.; Shaner, M.; Aggarwal, S.; Arent, D.; Azevedo, I. L.; Benson, S. M.; Bradley, T.; Brouwer, J.; Chiang, Y. M.; Clack, C. T. M.; Cohen, A.; Doig, S.; Edmonds, J.; Fennell, P.; Field, C. B.; Hannegan, B.; Hodge, B. M.; Hoffert, M. I.; Ingersoll, E.; Jaramillo, P.; Lackner, K. S.; Mach, K. J.; Mastrandrea, M.; Ogden, J.; Peterson, P. F.; Sanchez, D. L.; Sperling, D.; Stagner, J.; Trancik, J. E.; Yang, C. J.; Caldeira, K. Net-Zero Emissions Energy Systems. *Science* **2018**, *360*, No. eaas9793.

https://doi.org/10.1021/acsomega.4c06621
ACS Omega 2024, 9, 48374−48389

(34) Chen, Y. S.; Lin, C. C.; Lin, C. W.; Tsai, S. Y.; Ko, F. H. CsBr Immersion for Organic-Inorganic Hybrid Perovskite-Based Memristors: Controllable Grain, Poole-Frenkel Emission, and Electrical Properties. *ACS Appl. Electron. Mater.* **2023**, *5* (11), 5916−5927.
(35) Im, J. H.; Jang, I. H.; Pellet, N.; Grätzel, M.; Park, N. G. Growth of $CH_3NH_3PbI_3$ Cuboids with Controlled Size for High-Efficiency Perovskite Solar Cells. *Nat. Nanotechnol.* **2014**, *9*, 927−932.
(36) Li, B.; Binks, D.; Cao, G.; Tian, J. Engineering Halide Perovskite Crystals through Precursor Chemistry. *Small* **2019**, *15*, No. 1903613.
(37) Li, W.; Fan, J.; Li, J.; Mai, Y.; Wang, L. Controllable Grain Morphology of Perovskite Absorber Film by Molecular Self-Assembly Toward Efficient Solar Cell Exceeding 17%. *J. Am. Chem. Soc.* **2015**, *137* (32), 10399−10405.
(38) Hao, F.; Stoumpos, C. C.; Guo, P.; Zhou, N.; Marks, T. J.; Chang, R. P.; Kanatzidis, M. G. Solvent-Mediated Crystallization of $CH_3NH_3SnI_3$ Films for Heterojunction Depleted Perovskite Solar Cells. *J. Am. Chem. Soc.* **2015**, *137* (35), 11445−11452.
(39) Yao, H.; Peng, G.; Li, Z.; Wang, Q.; Xu, Y.; Ma, B.; Lei, Y.; Wang, G.; Wang, Q.; Ci, Z.; Zhang, H. L.; Jin, Z. Fine Coverage and Uniform Phase Distribution in 2D $(PEA)_2Cs_3Pb_4I_{13}$ Solar Cells with A Record Efficiency beyond 15%. *Nano Energy* **2022**, *92*, No. 106790.
(40) Li, B.; Shi, J.; Lu, J.; Tan, W. L.; Yin, W.; Sun, J.; Jiang, L.; Jones, R.-T.; Pigram, P.; Mcneill, C. R.; Cheng, Y. B.; Jasieniak, J. J. Facile Deposition of Mesoporous PbI_2 through DMF:DMSO Solvent Engineering for Sequentially Deposited Metal Halide Perovskites. *ACS Appl. Energy Mater.* **2020**, *3* (4), 3358−3368.
(41) Kialengila, D. M.; Wolfs, K.; Bugalama, J.; Van Schepdael, A.; Adams, E. Full Evaporation Headspace Gas Chromatography for Sensitive Determination of High Boiling Point Volatile Organic Compounds in Low Boiling Matrices. *J. Chromatogr. A* **2013**, *1315*, 167−175.
(42) Zhang, F.; Kim, D. H.; Lu, H.; Park, J. S.; Larson, B. W.; Hu, J.; Gao, L.; Xiao, C.; Reid, O. G.; Chen, X.; Zhao, Q.; Ndione, P. F.; Berry, J. J.; You, W.; Walsh, A.; Beard, M. C.; Zhu, K. Enhanced Charge Transport in 2D Perovskites via Fluorination of Organic Cation. *J. Am. Chem. Soc.* **2019**, *141*, 5972−5979.
(43) Zhang, C.; Zhang, Y.; Wang, X.; Shi, C.; Lin, Z.; Zhao, Z.; Zhao, D.; Li, M.; Chen, X. Modulation of Charge Transport from Two-Dimensional Perovskites to Industrial Charge Transport Layers by the Organic Spacer-Dependent Exciton-Phonon Interactions. *ACS Appl. Mater. Interfaces* **2023**, *15* (51), 59946−59954.
(44) Febriansyah, B.; Koh, T. M.; Lekina, Y.; Jamaludin, N. F.; Bruno, A.; Ganguly, R.; Shen, Z. X.; Mhaisalkar, S. G.; England, J. Improved Photovoltaic Efficiency and Amplified Photocurrent Generation in Mesoporous N = 1 Two-Dimensional Lead-Iodide Perovskite Solar Cells. *Chem. Mater.* **2019**, *31* (3), 890−898.
(45) Wang, Z.; Wang, F.; Zhao, B.; Qu, S.; Hayat, T.; Alsaedi, A.; Sui, L.; Yuan, K.; Zhang, J.; Wei, Z.; Tan, Z. Efficient Two-Dimensional Tin Halide Perovskite Light-Emitting Diodes via a Spacer Cation Substitution Strategy. *J. Phys. Chem. Lett.* **2020**, *11* (3), 1120−1127.
(46) Qing, J.; Kuang, C.; Wang, H.; Wang, Y.; Liu, X. K.; Bai, S.; Li, M.; Sum, T. C.; Hu, Z.; Zhang, W.; Gao, F. High-Quality Ruddlesden-Popper Perovskite Films Based on In Situ Formed Organic Spacer Cations. *Adv. Mater.* **2019**, *31*, No. 1904243.
(47) Chirvony, V. S.; Suárez, I.; Rodríguez, R. J.; Vázquez, C. R.; Sanchez-Diaz, J.; Molina-Sánchez, A.; Barea, E. M.; Mora-Seró, I.; Martínez-Pastor, J. P. Inhomogeneous Broadening of Photoluminescence Spectra and Kinetics of Nanometer-Thick $(Phenethylammonium)_2PbI_4$ Perovskite Thin Films: Implications for Optoelectronics. *ACS Appl. Nano Mater.* **2021**, *4* (6), 6170−6177.
(48) Yan, S. X.; Han, C. B.; Huang, J.; Chen, Y.; Zhang, X.; Chen, X.; Zhang, Y.; Yan, H. Organic Molecule Assisted Growth of Perovskite Films Consisting of Square Grains by Surface-Confined Process. *Nanomaterials* **2021**, *11* (2), 473.
(49) Song, Y.; Bi, W.; Wang, A.; Liu, X.; Kang, Y.; Dong, Q. Efficient Lateral-Structure Perovskite Single Crystal Solar Cells with High Operational Stability. *Nat. Commun.* **2020**, *11*, No. 274.
(50) Chen, S.; Goh, T. W.; Sabba, D.; Chua, J.; Mathews, N.; Huan, C. H. A.; Sum, T. C. Energy Level Alignment at the Methylammonium Lead Iodide/Copper Phthalocyanine Interface. *APL Mater.* **2014**, *2*, No. 081512.
(51) Hawash, Z.; Raga, S. R.; Son, D. Y.; Ono, L. K.; Park, N. G.; Qi, Y. Interfacial Modification of Perovskite Solar Cells Using an Ultrathin MAI Layer Leads to Enhanced Energy Level Alignment, Efficiencies, and Reproducibility. *J. Phys. Chem. Lett.* **2017**, *8* (17), 3947−3953.
(52) Hofstetter, Y. J.; García-Benito, I.; Paulus, F.; Orlandi, S.; Grancini, G.; Vaynzof, Y. Vacuum-Induced Degradation of 2D Perovskites. *Front. Chem.* **2020**, *8*, 66.
(53) Zhu, P.; Gu, S.; Luo, X.; Gao, Y.; Li, S.; Zhu, J.; Tan, H. Simultaneous Contact and Grain-Boundary Passivation in Planar Perovskite Solar Cells Using SnO_2-KCl Composite Electron Transport Layer. *Adv. Energy Mater.* **2020**, *10*, No. 1903083.
(54) Wei, J.; Guo, F.; Wang, X.; Xu, K.; Lei, M.; Liang, Y.; Zhao, Y.; Xu, D. SnO_2-in-Polymer Matrix for High-Efficiency Perovskite Solar Cells with Improved Reproducibility and Stability. *Adv. Mater.* **2018**, *30*, No. 1805153.
(55) Hui, W.; Yang, Y.; Xu, Q.; Gu, H.; Feng, S.; Su, Z.; Zhang, M.; Wang, J.; Li, X.; Fang, J.; Xia, F.; Xia, Y.; Chen, Y.; Gao, X.; Huang, W. Red-Carbon-Quantum-Dot-Doped SnO_2 Composite with Enhanced Electron Mobility for Efficient and Stable Perovskite Solar Cells. *Adv. Mater.* **2020**, *32*, No. 1906374.
(56) Chen, L.; Liu, Z.; Qiu, L.; Xiong, J.; Song, L.; Du, P. Multifunctional Regulation of SnO_2 Nanocrystals by Snail Mucus for Preparation of Rigid or Flexible Perovskite Solar Cells in Air. *ACS Nano* **2023**, *17* (23), 23794−23804.
(57) Wang, P.; Chen, B.; Li, R.; Wang, S.; Ren, N.; Li, Y.; Mazumdar, S.; Shi, B.; Zhao, Y.; Zhang, X. Cobalt Chloride Hexahydrate Assisted in Reducing Energy Loss in Perovskite Solar Cells with Record Open-Circuit Voltage of 1.20 V. *ACS Energy Lett.* **2021**, *6* (6), 2121−2128.
(58) Bu, T.; Li, J.; Zheng, F.; Chen, W.; Wen, X.; Ku, Z.; Peng, Y.; Zhong, J.; Cheng, Y. B.; Huang, F. Universal Passivation Strategy to Slot-Die Printed SnO_2 for Hysteresis-Free Efficient Flexible Perovskite Solar Module. *Nat. Commun.* **2018**, *9*, No. 4609.
(59) Liu, C.; Su, H.; Xie, K.; Wang, H.; Zhai, P.; Chang, N.; Zhang, S.; Ban, Q.; Guo, M.; Zhang, J.; Liu, L. Highly Enhanced Efficiency of Planar Perovskite Solar Cells by an Electron Transport Layer Using Phytic Acid-Complexed SnO_2 Colloids. *Sol. RRL* **2021**, *5*, No. 2100067.
(60) Ke, W.; Zhao, D.; Cimaroli, A. J.; Grice, C. R.; Qin, P.; Liu, Q.; Xiong, L.; Yan, Y.; Fang, G. Effects of Annealing Temperature of Tin Oxide Electron Selective Layers on the Performance of Perovskite Solar Cells. *J. Mater. Chem. A* **2015**, *3*, 24163−24168.
(61) Wang, C.; Wu, J.; Wang, S.; Liu, X.; Wang, X.; Yan, Z.; Chen, L.; Liu, X.; Li, G.; Sun, W.; Lan, Z. Alkali. Metal Fluoride-Modified Tin Oxide for n-i-p Planar Perovskite Solar Cells. *ACS Appl. Mater. Interfaces* **2021**, *13* (42), 50083−50092.
(62) Gong, X.; Sun, Q.; Liu, S.; Liao, P.; Shen, Y.; Grätzel, C.; Zakeeruddin, S. M.; Grätzel, M.; Wang, M. Highly Efficient Perovskite Solar Cells with Gradient Bilayer Electron Transport Materials. *Nano Lett.* **2018**, *18* (6), 3969−3977.
(63) Yang, D.; Yang, R.; Wang, K.; Wu, C.; Zhu, X.; Feng, J.; Ren, X.; Fang, G.; Priya, S.; Liu, S. F. High Efficiency Planar-Type Perovskite Solar Cells with Negligible Hysteresis Using EDTA-Complexed SnO_2. *Nat. Commun.* **2018**, *9*, No. 3239.
(64) Cao, Y.; Yang, W.; Zhang, W.; Liu, G.; Yue, P. Improved Photocatalytic Activity of Sn^{4+} Doped TiO_2 Nanoparticulate Films Prepared by Plasma-Enhanced Chemical Vapor Deposition. *New J. Chem.* **2004**, *28*, 218−222.
(65) Tran, Q. P.; Fang, J. S.; Chin, T. S. Properties of Fluorine-Doped SnO_2 Thin Films by a Green Sol-Gel Method. *Mater. Sci. Semicond. Process.* **2015**, *40*, 664−669.
(66) Xu, X.; Lin, Z.; Cai, Q.; Dong, H.; Wang, X.; Mu, C. Defect Management by a Cesium Fluoride-Modified Electron Transport

https://doi.org/10.1021/acsomega.4c06621
ACS Omega 2024, 9, 48374−48389

Layer Promotes Perovskite Solar Cells. *Phys. Chem. Chem. Phys.* **2022**, *24*, 22562−22571.
(67) Liang, J.; Chen, Z.; Yang, G.; Wang, H.; Ye, F.; Tao, C.; Fang, G. Achieving High Open-Circuit Voltage on Planar Perovskite Solar Cells via Chlorine-Doped Tin Oxide Electron Transport Layers. *ACS Appl. Mater. Interfaces* **2019**, *11* (26), 23152−23159.
(68) Yang, Y.; Liu, C.; Syzgantseva, O. A.; Syzgantseva, M. A.; Ma, S.; Ding, Y.; Cai, M.; Liu, X.; Dai, S.; Nazeeruddin, M. K. Defect Suppression in Oriented 2D Perovskite Solar Cells with Efficiency Over 18% via Rerouting Crystallization Pathway. *Adv. Energy Mater.* **2021**, *11*, No. 2002966.
(69) Saidaminov, M. I.; Abdelhady, A. L.; Murali, B.; Alarousu, E.; Burlakov, V. M.; Peng, W.; Dursun, I.; Wang, L.; He, Y.; Maculan, G.; Goriely, A.; Wu, T.; Mohammed, O. F.; Bakr, O. M. High-Quality Bulk Hybrid Perovskite Single Crystals within Minutes by Inverse Temperature Crystallization. *Nat. Commun.* **2015**, *6*, No. 7586.
(70) Han, Q.; Bae, S. H.; Sun, P.; Hsieh, Y. T.; Yang, Y. M.; Rim, Y. S.; Zhao, H.; Chen, Q.; Shi, W.; Li, G.; Yang, Y. Single Crystal Formamidinium Lead Iodide ($FAPbI_3$): Insight into the Structural, Optical, and Electrical Properties. *Adv. Mater.* **2016**, *28*, 2253−2258.
(71) Tang, X.; Chen, M.; Jiang, L.; Li, M.; Tang, G.; Liu, H. Improvements in Efficiency and Stability of Perovskite Solar Cells Using a Cesium Chloride Additive. *ACS Appl. Mater. Interfaces* **2022**, *14* (23), 26866−26872.
(72) Zheng, H.; Wu, W.; Xu, H.; Zheng, F.; Liu, G.; Pan, X.; Chen, Q. Self-Additive Low-Dimensional Ruddlesden-Popper Perovskite by the Incorporation of Glycine Hydrochloride for High-Performance and Stable Solar Cells. *Adv. Funct. Mater.* **2020**, *30*, No. 2000034.
(73) Li, Z.; Gao, Y.; Zhang, Z.; Xiong, Q.; Deng, L.; Li, X.; Zhou, Q.; Fang, Y.; Gao, P. cPCN-Regulated SnO_2 Composites Enables Perovskite Solar Cell with Efficiency beyond 23%. *Nano−Micro Lett.* **2021**, *13*, 101.
(74) Ramakrishnan, S.; Li, H.; Xu, Y.; Shin, D.; Dursun, I.; Cotlet, M.; Zhang, Y.; Yu, Q. Ruddlesden-Popper Perovskites with Narrow Phase Distribution for Air-Stable Solar Cells. *Sol. RRL* **2022**, *6*, No. 2200490.
(75) Ouedraogo, N. A. N.; Odunmbaku, G. O.; Guo, B.; Chen, S.; Lin, X.; Shumilova, T.; Sun, K. Oxidation of Spiro-Ometad in High-Efficiency Perovskite Solar Cells. *ACS Appl. Mater. Interfaces* **2022**, *14* (30), 34303−34327.

https://doi.org/10.1021/acsomega.4c06621
ACS Omega 2024, 9, 48374−48389